J. Fluid Mech. (2021), *vol*. 918, A8, doi:10.1017/jfm.2021.323

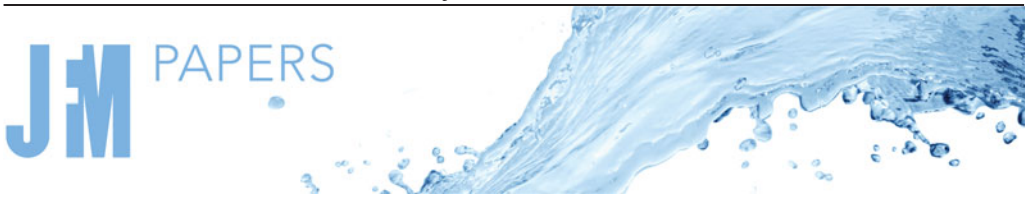

Effect of tabs on transverse jet instabilities, structure, vorticity dynamics and mixing

Elijah W. Harris[1], **A.C. Besnard**[1] **and A.R. Karagozian**[1,†]

[1]Department of Mechanical and Aerospace Engineering, University of California, Los Angeles, Los Angeles, CA 90095, USA

(Received 6 October 2020; revised 18 March 2021; accepted 7 April 2021)

This experimental study examined the effects of strategic positioning of tabs in the periphery of the exit plane of a transverse jet as a means of controlling shear layer instabilities and vorticity as well as jet structure and mixing. Conditions corresponding to a naturally absolutely unstable upstream shear layer (USL), with low jet-to-crossflow momentum flux ratios J (below 8–9) and to a convectively unstable USL ($J \geq 20$) were explored for different jet Reynolds numbers, 1900 and 2300. Acetone planar laser-induced fluorescence imaging and stereo particle image velocimetry were utilized to explore the influence of the tab. Placement of the tab in the upstream region of the jet exit caused significant weakening of the USL instability at lower J, but with only marginal weakening for larger J values. Yet tab placement was observed to affect cross-sectional structure and vorticity dynamics much more significantly at high J values. For all flow conditions, tab placement in the upstream region improved molecular mixing to a greater degree than at other locations. Vorticity fields, proper orthogonal decomposition modes, and coefficient plots extracted from centreplane velocity field measurements showed significant influence of tab placement on jet dynamical characteristics depending on J. Tab locations with the greatest influence were consistent with wavemaker regions predicted in numerical simulations of the transverse jet (Regan & Mahesh, *J. Fluid Mech.*, vol. 877, 2019, pp. 330–372), providing evidence for the potential to tailor shear layer rollup, jet structure and mixing via simple passive geometrical alterations.

Key words: absolute/convective instability, jets, shear layers

1. Introduction

The jet in crossflow (JICF) or transverse jet has been studied over the years for its myriad applications, especially for aircraft and rocket propulsion systems (Margason 1993; Karagozian 2010; Mahesh 2013). In each of these applications the desired characteristics

† Email address for correspondence: ark@seas.ucla.edu

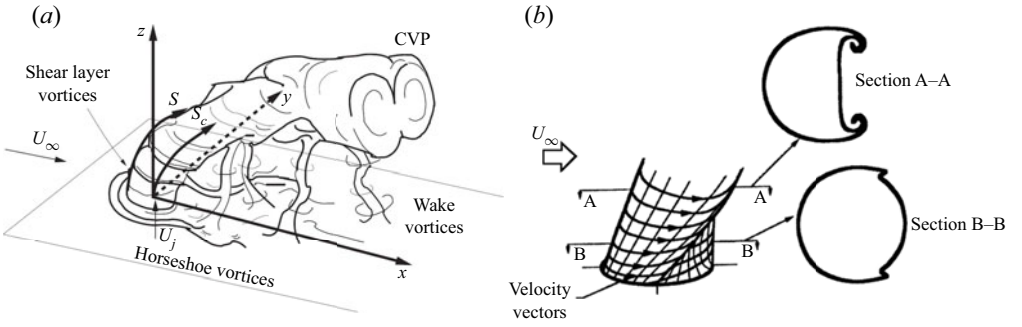

Figure 1. (*a*) Schematic of a flush round jet injected normally into crossflow, with representative depictions of the relevant vortical structures. Coordinate axes x, y, z, jet shear layer trajectory s, and jet centreline trajectory s_c are also shown. Adapted from Fric & Roshko (1994). (*b*) Depiction of a reorientation of the shear layer vorticity leading to formation of the CVP. From Kelso *et al.* (1996).

of the JICF differ, ranging from deep penetration and efficient mixing between the jet and crossflow to reduced penetration for surface cooling applications. The resulting flow system is quite complex and highly three-dimensional, yielding a rich topology of vortical structures and nonlinear dynamics, the understanding of which can assist in developing strategies for control of the structural, mixing and stability characteristics.

Figure 1(*a*) schematically depicts the round jet injected normally into a uniform crossflow, which results in a complex three-dimensional flow topology rich in vortical systems and flow structures. The flow field is composed of a horseshoe vortex which wraps around the jet column, shear layer vortices which periodically form and evolve along the upstream shear layer (USL) of the jet, upright columnar wake vortices bound between the wall boundary layer and the downstream portion of the jet, and a counter rotating vortex pair (CVP) which dominates the jet cross-section (Kamotani & Greber 1972; Kelso, Lim & Perry 1996; Cortelezzi & Karagozian 2001). Some of the common non-dimensional parameters utilized to characterize this flow field are the jet-to-crossflow velocity ratio ($R = U_j/U_\infty$), jet-to-crossflow density ratio ($S = \rho_j/\rho_\infty$), jet-to-crossflow momentum flux ratio ($J = \rho_j U_j^2/\rho_\infty U_\infty^2 = SR^2$) and jet Reynolds number ($Re_j = \rho_j U_j D/\mu_j$), which is based on the jet exit diameter (D), bulk velocity (U_j) and absolute viscosity of the jet mixture (μ_j). When considering the instability characteristics of the USL, the frequency content (f) can be non-dimensionalized using a Strouhal number, $St = fD/U_j$, based on the jet diameter; relevant Strouhal numbers can also be defined in terms of the jet's upstream momentum thickness (θ) (Shoji *et al.* 2020*b*).

A long held understanding of the JICF has been the significance of the CVP to the efficacy of mixing between the jet and crossflow (Kamotani & Greber 1972; Fearn & Weston 1974). Increased CVP coherence, strength and symmetry have been demonstrated to result in better molecular mixing of the jet (Gevorkyan *et al.* 2016). The formation and strength of the CVP structure has been proposed to originate from the initiation of azimuthal vorticity in the form of vortex rings along the shear layer of the jet which are subsequently reoriented by tilting and folding due to the influence of the crossflow (Kelso *et al.* 1996; Cortelezzi & Karagozian 2001), as suggested in figure 1(*b*). By tracking vortex filaments emanating from the jet exit, Marzouk & Ghoniem (2007) note that there is a distinct difference in the rollup along the windward and leeward sides of the jet, where the leeward side is delayed or stretched downstream due to an induced upward velocity from the leeside portion of the vortex ring. As the leeside is stretched it leads to upright

vortex arms which align with the jet trajectory and are counter-rotating in nature. Earlier three-dimensional vortex element analysis by Cortelezzi & Karagozian (2001) shows that the degree of interaction or coupling between successive vortex rings, the respective periodicity of the rings, and their resulting impact on the CVP are dependent on initial conditions such as the jet velocity, crossflow velocity and the upstream boundary layer thickness.

Given the intimate coupling between the CVP formation and shear layer vortices, there has been a good deal of interest in the dynamics of shear layer evolution, explored through experimental (Megerian *et al.* 2007; Davitian *et al.* 2010*a*), numerical (Bagheri *et al.* 2009; Schlatter, Bagheri & Henningson 2011; Iyer & Mahesh 2016; Regan & Mahesh 2017) and theoretical (Alves, Kelly & Karagozian 2007; Ilak *et al.* 2012) investigations. The experiments of Megerian *et al.* (2007), which utilize a fifth-order polynomial nozzle with an exit diameter of 4.04 mm, are the first to show that for a flush equidensity JICF, as the velocity ratio (R) is systematically decreased with a fixed jet Reynolds number, the USL flow field exhibits a transition from convective instability to an absolute or global instability when R falls below approximately 3.3 (or $J < 10$). Direct numerical simulations (DNS) of this same nozzle and JICF flow field by Iyer & Mahesh (2016) confirm the same USL instability characteristics as in the experiments, both qualitatively and quantitatively, at convectively unstable (CU) conditions for $R = 4$, and absolutely unstable (AU) conditions for $R = 2$. Subsequent experimental work by Davitian *et al.* (2010*a*) with the same configuration shows that for strongly AU USL flow conditions, at $R \lesssim 3.0$, the dominant USL instability frequency is also detected along the sides and even in the leeside region of the jet, though in the latter the instability is significantly weaker. When the USL is CU at a slightly higher R value, $R = 3.3$, the USL instability is weaker, yet the dominant frequency is also detected at the sides of the jet, but not in the leeside spectra, which contain a series of much lower frequencies. Differences in the shear layer stability characteristics around the transverse jet periphery are also documented in the global linear stability analysis by Regan & Mahesh (2017), who observe for the JICF with an AU USL at $R = 2$ that the dominant eigenmode lies along the USL of the jet, but for the case with a CU USL at $R = 4$, downstream shear layer instabilities are shown to dominate. Interestingly, for the AU jet, the second dominant eigenmode is seen to originate along the downstream shear layer, having an order of magnitude lower frequency and a growth rate that is approximately half that of the dominant mode.

Relating these instability characteristics to the development of the jet structure and especially the jet cross-section for the round JICF, Getsinger *et al.* (2014) employed acetone planar laser-induced fluorescence (PLIF) imaging to show that an initially CU USL at large R or J values becomes even more weakly CU along the jet trajectory, and the attendant weakening of the USL rollup creates susceptibility to the influence of asymmetric disturbances and imperfections in the experimental configuration, especially in the crossflow, ultimately leading to the formation of an asymmetric CVP in the cross-section. These asymmetric structures contrast the relatively symmetric, clear CVP structure that dominates the jet cross-section at lower momentum flux ratios or velocity ratios corresponding to an AU USL. Other experimental studies also document asymmetries in the transverse jet cross-section at relatively high momentum flux ratios (Kuzo 1995; Smith & Mungal 1998; Shan & Dimotakis 2006), or for the JICF with a relatively short orifice (Peterson & Plesniak 2004), where there can be symmetry breaking taking place upstream of the jet injection plane. Hence, the nature and strength of the shear layer instabilities, even at different locations about the jet periphery, and the evolution of instabilities along both the upstream and downstream shear layers, have an important

influence on jet structural evolution, and motivate the exploration of selective alterations to the shear layer at specific azimuthal orientations about the jet.

Despite the JICF's classification as an efficient mixer, depending on flow conditions (Gevorkyan *et al.* 2016), there have been numerous efforts over the years to further improve the efficacy of mixing through passive and/or active control of the jet. While active control involves temporal variation in flow parameters, with the potential for sensor-based feedback or feedforward control (M'Closkey *et al.* 2002; Davitian *et al.* 2010*b*; Shoji *et al.* 2019), passive control typically is simpler to employ, for example, with a fixed geometrical change jet shape (Haven & Kurosaka 1997). Among the passive control measures that have seen relatively limited exploration are those with an alteration in the jet exit profile due to the presence of small tabs or vortex generators placed about the jet exit. For the free jet, such tabs can demonstrate remarkable enhancement of entrainment and jet mixing (Bradbury & Khadem 1975; Ahuja & Brown 1989; Zaman, Reeder & Samimy 1992; Carletti, Rogers & Parekh 1996). Ahuja & Brown (1989) and Zaman, Reeder & Samimy (1991) show that the placement of small flush tabs at the injector exit can act to azimuthally excite the flow and enhance streamwise vorticity generation. Zaman, Reeder & Samimy (1994) and Bohl & Foss (1995) further suggest through experimental observations that the vorticity generation from a tabular protrusion into the jet flow originates from two sources: a 'pressure hill' upstream of the issuing tab, and shed vortex sheets from the sides of the tab.

For the transverse jet, given the sensitivity of the CVP and the shear layer vortices to the initial jet flow conditions, the utilization of a tab at the jet exit could well provide advantageous alterations to the flow field and mixing characteristics. In the earliest studies of a tabbed JICF, a small tab is placed on the downstream/lee side of the jet exit so that the proposed net vorticity production from the tab would align with and enhance the circulation of the CVP, thereby potentially improving the mixing (Liscinsky, True & Holdeman 1995; Zaman 1998). However, these investigations ultimately show that for a range of jet Reynolds numbers ($Re_j = 24\,000$–$54\,000$), and multiple momentum flux ratios ($J = 8.5$, 21, and 54), the tab is actually ineffective and has negligible influence on the flow field when placed on the downstream side of the jet. In contrast, Zaman & Foss (1997) find that for the same flow conditions, placement of a tab in the upstream edge of the jet periphery is able to alter the jet, where the penetration and strength of the CVP are both significantly reduced. They theorize the differences in effectiveness between tab orientations is attributable to a lower static pressure on the downstream side of the jet, resulting in a reduced tab vorticity generation from the pressure-hill source when positioned downstream. The implications of tab placement about the periphery of the JICF are explored in greater detail by Bunyajitradulya & Sathapornnanon (2005), who examine a single tab positioned at eight different azimuthal orientations for a heated JICF with fixed flow conditions corresponding to $S = 0.86$, $J = 16$ and $Re_j = 15\,000$. They observe the strength of alterations to the jet to be systematically diminished as the tab orientation transitions from the upstream edge towards the downstream, at which point little to no impact from the tab is seen. Interestingly, tabs that are positioned at locations other than at the upstream or downstream positions are able to produce a skewing of the jet cross-sectional symmetry. A more recent experimental study on the effects of two small oscillating tabs oriented at streamwise positions at the jet exit (Zaman & Milanovic 2012) at a jet Reynolds number of 57 000 indicates the potential for temporal creation of asymmetric cross-sectional structures at large momentum flux ratios, e.g. $J = 48$, though the flow does not respond to the tab oscillation when J is less than 15.

Studies examining a tabbed JICF have not extensively explored the implications of fixed tab orientation on the mixing characteristics of the jet, and the only one that has done so

explores flows at relatively high momentum flux ratios, $J > 20$, and jet Reynolds numbers, $Re_j > 24\,000$ (Liscinsky *et al.* 1995). Understanding JICF mixing characteristics over a range of flow regimes is not only of practical importance, but it is of great interest to understand the impact of a tab on the previously mentioned USL instabilities given the significance of the instability characteristics to the development of the CVP and associated molecular mixing (Gevorkyan *et al.* 2016). The present experimental study seeks to investigate these tab effects on transverse jet USL stability characteristics, the associated jet structure and resultant molecular mixing characteristics. Additionally, the means by which the tabs themselves alter the vorticity field at the exit, and, hence, the shear layer rollup, are of interest, given the importance of the eventual CVP development to mixing enhancement. Stereo particle image velocimetry (PIV) in the experiments, simultaneous to acetone PLIF, can answer such questions. Further, proper orthogonal decomposition (POD) of such imaging can assist with understanding the dynamical character of the flow field and modifications that can be created even by simple passive structures. Such explorations can also help to explain observations made in other much earlier studies.

2. Experimental set-up and methods

2.1. *Transverse jet tunnel*

The experiments in this study were conducted in the low speed wind tunnel shown schematically in figure 2. The tunnel has room air continually drawn from the laboratory through a centrifugal blower and later exhausted through ducting to the building exhaust. Air from the blower was conditioned through a series of mesh screens and honeycomb cells before entering a contraction with a 9 : 1 area ratio, which fed directly into the main test section. Measurements of the free-stream velocity field within the tunnel yielded turbulence intensity levels of less than 1.5 %, with maximum attainable velocities of $U_\infty \approx 7.0$ m s^{-1}. The main test section consisted of a 12 cm $\times$ 12 cm $\times$ 82.5 cm black anodized aluminium chamber. The side walls were fitted with Plexiglas to provide optical access to the cameras, while the top of the tunnel was fitted with a fused silica quartz window which passed the UV and green laser light into the chamber for illumination of the jet during acetone PLIF imaging and stereo PIV measurements. In addition to the black anodize, the tunnel floor was also coated with a matte black heat-resistant paint to further mitigate the reflections and ablation created by laser light at the surfaces. To minimize any attenuation of the flow field due to a pressure drop from the suction of the exhaust, a 30 cm $\times$ 30 cm $\times$ 63 cm dissipating chamber was affixed to the end of the tunnel section.

The main tunnel floor was fitted with a removable section, the leading edge of which was 3.8 cm downstream of the termination of the tunnel contraction and with an exposed surface of 9.3 cm by 22.3 cm; alternative versions of the removable section are shown in figure 3. Mounting to the main tunnel floor was made via a 0.6 cm lap joint, with supporting stanchions placed beneath to anchor the removable piece in place, ensuring a tight seal about the seams. Measurements of the crossflow boundary layer and turbulence levels confirmed that crossflow characteristics, such as wall boundary layer thickness variation with flow conditions, were consistent with those in prior studies in this tunnel (Megerian *et al.* 2007; Getsinger *et al.* 2014; Gevorkyan *et al.* 2016). The removable flooring allowed for easy changes to the flow-field configuration, between the original unaltered JICF (figure 3*a*), with a fitting into which the original round jet nozzle was secured, and the tabbed JICF (figure 3*b*), into which a template (with or without a tab) could be placed. The floor designed for the tabbed jet made use of a small recession in the floor to accommodate the thickness of the template affixed to the end of the jet nozzle,

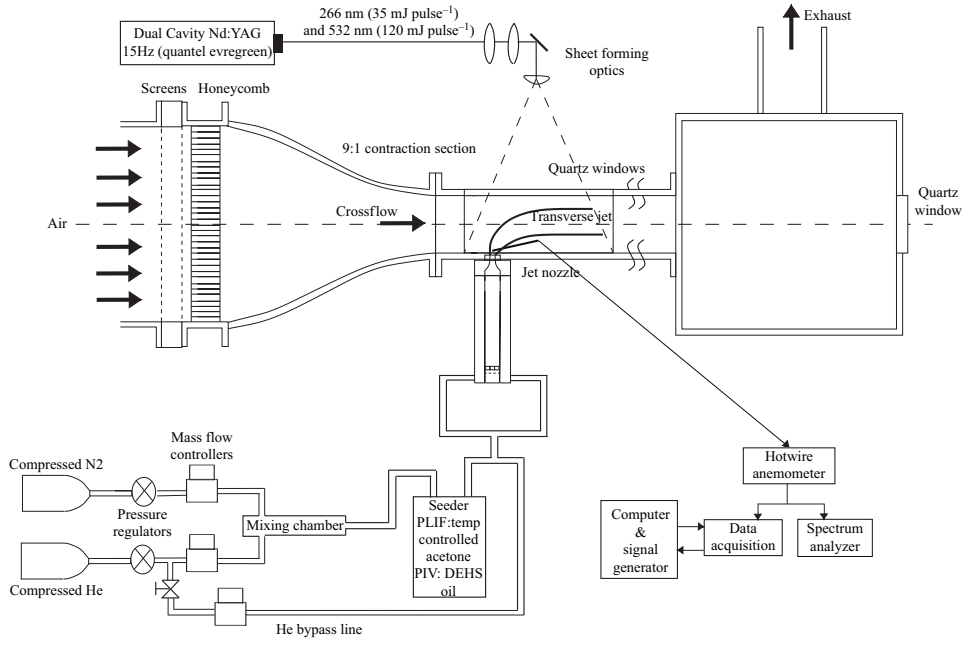

Figure 2. Low speed wind tunnel, laser system, hotwire anemometry and variable density jet injection and seeding system comprising the experimental JICF set-up.

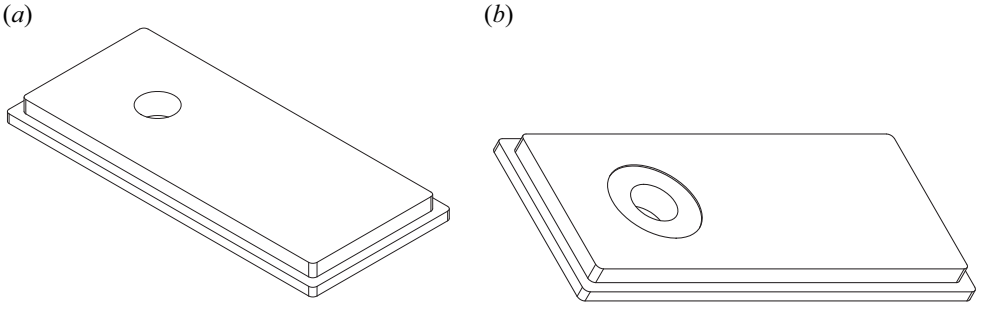

Figure 3. Computer-aided design drawings for the removable floors integrated into the main wind tunnel for investigation of different jet geometries: (*a*) plain flush mounted jet injection floor for the unforced jet studied in prior experiments, and (*b*) recess-mounted jet floor for passive control of the jet via tabs.

while keeping the resulting jet exit plane flush with the tunnel floor. Below the bottom of the nozzle fitting was a PVC pipe of sufficient length for full development of laminar pipe flow at the entrance to the nozzle, alleviating any asymmetries associated with the inlet fittings (Gevorkyan *et al.* 2018).

The tab geometry used here was based on findings in prior free jet experiments (Bradbury & Khadem 1975; Zaman *et al.* 1994; Carletti *et al.* 1996) as well as JICF testing (Zaman 1998). In the present experiments the tab consisted of a simple triangular protrusion oriented coplanar with the tunnel floor, where the base tab length of 1/4 jet diameters resulted in an effective jet flow blockage of approximately 4 %. The template in which the tab was machined is shown in figure 4(*a*), with an outer diameter of the disc equal to 5 cm; the circular opening into which the tab was machined had the same diameter as the jet nozzle, 4.04 mm. A magnified view of the tab within the orifice template is shown

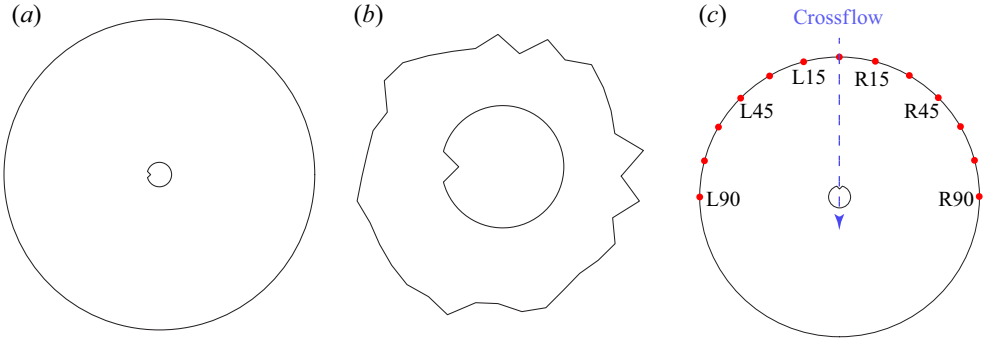

Figure 4. (*a*) Computer-aided design drawing of the single triangular tab insert with an approximate flow blockage of 4 %. (*b*) Magnified depiction of the jet orifice with tab protrusion for the single tab insert. (*c*) Depiction of tab orientation relative to oncoming crossflow.

in figure 4(*b*). The design of the template was such that the tab position could be rotated to any azimuthal position desired relative to the oncoming crossflow. Labelling for the various tab positions is shown in figure 4(*c*). An additional template, of the same thickness (0.813 mm) as the tabbed template, but with only a round opening of diameter 4.04 mm, was also used in the present experiments. This enabled a more accurate comparison of the influence of the tab on the JICF as compared with the jet without a tab but with an extension of the same thickness. There were small differences in the USL characteristics between the original flush nozzle and that of the nozzle with the small tabless extension, with the latter USL being slightly weaker than the former. While the differences were not very large, from the perspective of the shear layer dynamics and velocity/vorticity field, it was important to have a direct comparison in the present studies.

The jet's constituent species consisted of helium, nitrogen, acetone vapour and di-ethyl-hexyl-sebacat (DEHS) oil, where the latter two species served as the traces for acetone PLIF and PIV diagnostics, respectively. The specific determination of the bulk jet flow properties were based on calculations utilizing the mole fractions of the constituent species, room temperature and room pressure, which are detailed in Gevorkyan (2015). Flow rates for the He and N_2 were independently fixed by mass flow controllers (Tylan Model FC-260), and when performing simultaneous PLIF and PIV measurements an additional controller (MKS GM50A) was utilized for a secondary supply of N_2 to allow for independent seeding of both tracer particles. For such experiments, the mixture of N_2 and He flowed into a temperature-controlled acetone seeder, which was maintained in the vapour phase. Adjusting the mole fractions of various species enabled the desired density and jet Reynolds number to be achieved (Gevorkyan *et al.* 2016, 2018). Jet density and viscosity were calculated considering all constituents in the jet, depending on experimental conditions. Importantly, the mole fraction of acetone was determined such that at room temperature and pressure it would be below the critical saturated vapour concentration so as to prevent condensation of acetone.

A range of flow conditions were explored in these experiments, some for the high-resolution acetone PLIF imaging, and other cases in which the simultaneous PLIF and PIV imaging was performed. For the high-resolution PLIF imaging, the jet fluid had mole fractions of 0.218, 0.234 and 0.548 for the acetone, He and N_2, respectively. The flow rates were fixed so the resulting jet, in the absence of a tabbed insert, had a jet-to-crossflow density ratio of $S = 1$, and a jet Reynolds number of $Re_j = 2300$, with a jet bulk velocity of $U_j = 7.91$ m s^{-1}. Results for two momentum flux ratios are shown here, for the AU $J = 7$

and the CU $J = 61$. For the simultaneous imaging, the mole fractions of acetone, He and N_2 were set at 0.112, 0.100 and 0.788, respectively, to account for the additional DEHS oil seeding while still maintaining a density ratio of $S = 1$. The simultaneous imaging experiments produced a jet Reynolds number of $Re_j = 1900$, with a bulk jet velocity of $U_j = 6.80$ m s^{-1}. In this investigation the momentum flux ratios ranged from $J = 5$ to 41. For both the high-resolution PLIF and simultaneous PLIF and PIV imaging, the momentum flux ratio was altered through changes in the crossflow velocity U_∞, while keeping the jet flow fixed.

2.2. *Diagnostics*

Evaluation of the evolution of spectral characteristics along the USL of the jet was made with a single-component constant temperature hotwire anemometry probe (Dantec 55P15). The probe traversed along the USL and measured the vertical velocity fluctuations. The readings were sent to a 90C10 constant temperature anemometry module in a Dantec StreamLine 90N10 frame, after which the signal was split into AC and DC components and conditioned through a system created by Hendrickson (2012). The conditioned AC signal was then fed into a dynamic signal analyser (HP-35665A), where the power spectra were extracted over a span of 6.4 kHz at an 8 Hz resolution. The hotwire probe was able to translate in the x, y and z directions with an accuracy of 1 μm (2.48×10^{-4} jet diameters) via a triple axis traversing platform consisting of Newport high-performance low-profile ball-bearing linear stages. Details regarding the determination of the shear layer trajectory, calibration of the hotwire probe and other aspects of the hotwire may be found in Shoji (2017).

The present experiments also explored jet characteristics via non-intrusive optical diagnostics, acetone PLIF imaging and stereo PIV, as indicated in figure 2. The light source for both diagnostics was a dual-cavity Q-switched Nd:YAG laser (Quantel Evergreen 30266) operating at wavelengths of 532 nm (visible green) and 266 nm (UV). The laser cavities were independently tunable so as to match the energy output between them to yield similar particle illumination between snapshots, thereby helping to promote accurate extraction of velocity vectors from the PIV, especially with respect to the out-of-plane velocity when resolving all three velocity components in stereo PIV. Each cavity was capable of producing laser pulses at 8 ns full width at half-maximum with UV and green energy levels of approximately 30 mJ and 200 mJ, respectively. While the maximum repetition rate of the dual pulsed laser was 15 Hz, the experiments were all conducted at a rate of 5 Hz so as to maximise the signal-to-noise ratio (SNR) of the UV to green light, as well as prevent excessive ablation and reflections at the laser floor from the higher energy green light. The repetition rate, time increment between the cavities and timing of the laser relative to the cameras were all controlled by a programmable external timing unit and LaVision's DaVis 8.2 software. All recorded data sets consisted of 500 instantaneous realizations of the flow field which were not phase-locked or phase-progressing with the natural dynamics of the flow field. This number of realizations was more than sufficient to provide statistical convergence of the examined metrics (Shoji 2017).

2.2.1. *High-resolution PLIF*

For the high-resolution acetone PLIF imaging, which enabled more accurate determination of molecular mixing characteristics, the collimated laser beam was passed through two dichroic mirrors to split the UV component from the green. The UV light was then passed through a UV-grade fused silica window which reflected a portion of the laser (≈7 %) to

a pyroelectric joulmeter (Newport 818E-10-50-S) for shot-to-shot energy measurements, utilized later in imaging post-processing. The remaining beam passed through a focusing optic and a turning mirror to direct the beam into the test section. An $f = -10$ mm cylindrical lens spread the beam into a sheet and could be rotated to provide imaging of the jet centreplane or the cross-section. The resulting laser sheet thickness was quantified using the knife-edge traversal technique, and was found to be $\approx$1 mm over the entire field of view (FOV).

Images were recorded with a 14-bit charge coupled device (CCD) camera (LaVision Imager proX) with image resolution of 1600 $\times$ 1200 pixels. An external image intensifier (LaVision IRO) was used to improve the SNR. Centreplane images were taken with a Nikon 500 lens at f/2.0 with a Vivitar +2 dioptre close-up lens, while in the cross-section a Nikon 200 mm lens at f/4.0 was implemented. In both cases a bandpass filter was also utilized to isolate the flourescence signal. Data sets consisted of 500 instantaneous snapshots, well above the number required to achieve statistical convergence of the image data (Shoji 2017). Post processing of the images included 2 $\times$ 2 binning, noise bias correction, flat-field correction, background subtraction, laser energy absorption correction and a dual-pass filtering. Details regarding these processes, and representative effects on the images, are documented in Shoji (2017). The imaging FOV and final processed resolution provided pixel sizes in the range of 60–100 μm for both centreplane and cross-sectional views. Prior work by Gevorkyan *et al.* (2018) shows that, for this diffusion dominated flow field, the spatial resolution of the PLIF images was sufficiently resolved, being well below the conservative estimate of the strain-limited diffusion scale ($\lambda_d \approx 350\mu$m), per Su & Mungal (2004).

2.2.2. *Simultaneous PLIF and PIV*

For the simultaneous imaging, both the UV and green light were preserved. The collimated laser beam was passed through a focusing optic before being turned and spread into a thin sheet by a UV coated $f = -10$ mm cylindrical lens, which was able to be rotated such that the sheet was in the centre or cross-sectional planes of the jet. Setting the time increment (dt) between pulses from the two cavities was determined by inspection of particle translation within the flow field which would yield accurate velocity vectors without losing the particles to out-of-plane motion. The resulting laser sheet thickness was maintained slightly thicker than for the high-resolution PLIF imaging, at $\approx$1.4 mm over the entire FOV, so as to mitigate the loss of particles to out-of-plane motion.

The PLIF images were recorded with a 12-bit internally intensified CCD camera (LaVision NanoStar) with image resolution of 1280 $\times$ 1040 pixels. This contrasts the high-resolution PLIF-only experiments which had an image resolution of 1600 $\times$ 1200 pixels. The internal intensifier operated at a gate time of 200 ns, corresponding to an exposure time that was 1 % of the lifetime for phosphorescence of acetone molecules. During the gated image exposure time, both of the Nd:YAG laser cavities would pulse, thereby effectively enhancing the energy of incident laser within the FOV by a factor of two, while not introducing any temporal smearing of the fluorescence signal. Careful consideration of the temporal spacing was required so that nonlinear interaction between the two pulses resulting in destructive interference and a decrease in energy output was not generated. In the centreplane (x–z plane), images were taken with a Sigma 90 mm AF at $f/2.8$ accompanied by a Vivitar +2 dioptre close-up lens. Additionally, a bandpass filter was implemented to isolate light in the acetone fluorescence spectrum from that of other irradiated background light. The images were post-processed through the same steps as the higher-resolution imaging, except that the shot-to-shot energy corrections were not able to

be implemented due to the remaining presence of the green light. Due to the presence of smoke and DEHS oil particles within the flow for PIV measurements, and additional light contamination from the green laser sheet, the resulting images and statistics extracted from them were of lower quality than isolated high-resolution PLIF-only imaging.

For the PIV measurements, the DEHS oil ($C_{26}H_{50}O_4$, LaVision 1108951) was seeded to the jet flow and, as is commonly done, was assumed to participate at such a low seeding density that it was a neutral participant in the overall flow properties of the jet. In order to visualize and quantify the velocity field of the crossflow as well as the jet, the crossflow was seeded with glycol-based smoke particles (0.2 μm mass-median diameter) by a commercial grade fog machine (Pea Soup Rocket) just outside of the centrifugal blower. The laser sheet thickness was established at about ≈1.2 mm over the entire FOV as determined by the knife-edge technique. The sheet thickness was formatted such that it was sufficiently thin enough to be considered a planar measurement field, while yet thick enough to capture out-of-plane motion of the particles for stereo PIV assessment.

Stereoscopic PIV images were collected by two 14-bit cross-correlated CCD cameras (LaVision Imager ProX) which were placed on either side of the NanoStar camera utilized for the PLIF imaging. The two cameras were oriented through the side optical window of the tunnel, at angles displaced from perpendicular to the zx-plane of approximately 22.5°, with the resulting offset yielding a 45° separation between the two cameras. Mounted to each camera was a Nikon 60 mm lens at $f/11.0$, coupled with a 532.5 nm narrowband filter. To assist in the fine tuning of the imaging a Scheimpflug lens mount (LaVision 1108196 version 1) was integrated with the lenses, allowing for tilting of the lens plane relative to the CCD array so as to maintain focus over the entire domain. Determination of velocity vectors from the particle displacements was performed by processes self-contained within LaVision's DaVis 8.2 software. User defined parameters afforded the selection of vector calculations via a multi-pass stereo cross-correlation with a decreasing window sizing of interrogation for improved accuracy (two passes at 32 × 32 pixel interrogation area at a 50 % overlap, and four passes at 24 × 24 pixel area at a 75 % overlap).

2.3. *Mixing quantification*

There have been a variety of methods implemented over the years to quantify the efficacy of mixing with the JICF. Historically these methods include averaged metrics for the jet such as spread, penetration and jet centreline concentration decay (Smith & Mungal 1998). It is noted, however (Shan & Dimotakis 2006), that the mixing processes in transitional or turbulent flow fields are inherently unsteady, and quantifications derived from such time-averaged evaluations could potentially wash-out some of the important instantaneous features relevant to molecular mixing. In the recent work of Gevorkyan *et al.* (2016) for a JICF, an extensive investigation of various mixing metrics indicates that molecular mixing can be accurately quantified via statistics associated with the second moment or variance of the scalar field, as can be quantified via the unmixedness parameter. Unmixedness can be represented by the following equation, for example, associated with a thin slice of a centreplane PLIF image, in the x–z plane, at downstream location x:

$$U = \frac{1}{L_x L_z} \iint \frac{\left(\dfrac{C}{C_o} - \dfrac{\bar{C}}{C_o}\right)^2}{\dfrac{\bar{C}}{C_o}\left(1 - \dfrac{\bar{C}}{C_o}\right)} \,\mathrm{d}x\,\mathrm{d}z. \tag{2.1}$$

Here C represents a local pixel element concentration (e.g. the pixel value associated with acetone fluorescence imaging) within an instantaneous jet image; $\bar{C}$ represents the spatially averaged concentration over the entire interrogation area; C_o is the concentration value at the jet exit, in the potential core region, which is applied as a scaling factor; and $L_x L_z$ represent the physical size of the interrogation area where the analysis is being performed, in this case, a thin (7 pixel-wide) slice of the jet in its centreplane. It should be noted that, to accomplish direct and meaningful comparisons of mixing metrics in the present experiments, the size of the cross-sectional interrogation area needed to be adjusted such that the mean value of the scalar over this area, $\bar{C}$, was matched at different locations along the jet, at different instants of time and among different jet flow conditions. Such spatial mean matching was administered here by adding or subtracting zero-valued pixels to create the same mean at all interrogation regions in the flow field. Unmixedness calculations were then applied to each instantaneous image and averaged over the number of realizations at a given location, producing an evaluation of local unmixedness as a function of downstream distance x. With this mixing metric, lower unmixedness values then correspond to improved relative molecular mixing. Given that the JICF flow field was highly three-dimensional and that there typically was a complex jet structure away from the centreplane, cross-sectional unmixedness was also quantified in the y–z plane for multiple downstream locations x. In many cases, as documented for both the unforced JICF (Gevorkyan *et al.* 2016) and the acoustically excited transverse jet (Shoji *et al.* 2019, 2020*a*), trends between the centreplane and cross-sectional mixing are quite similar, with exceptions typically corresponding to highly asymmetric jet cross-sections. Greater details regarding the unmixedness parameter and procedures for its implementation, along with details on other mean and instantaneous mixing metrics applied to the JICF are given in Gevorkyan (2015) and Shoji (2017).

3. Results

3.1. *Shear layer instability characteristics*

As noted, for a flush nozzle-injected JICF, the instabilities along the USL of the jet undergo a transition from convective instability to absolute/global instability as the jet-to-crossflow momentum flux ratio J is lowered below a critical threshold J_{cr} (Megerian *et al.* 2007; Davitian *et al.* 2010*a*; Getsinger, Hendrickson & Karagozian 2012). More recently, Shoji *et al.* (2020*b*) observed that even very small changes in the jet constituent species, causing a change in the bulk viscosity of the jet mixture, for example, due to the presence of acetone, can alter this transition point if other non-dimensional parameters such as J, Re_j and S remain fixed. Such changes in the jet-to-crossflow viscosity ratio require small changes to the mean jet velocity, and as a result alter the jet momentum thickness at the nozzle exit, which is noted by Megerian *et al.* (2007) and Alves, Kelly & Karagozian (2008) to play a significant role in the developing shear layer instabilities, as is the case in other shear layer instabilities (Michalke 1971). Experimentally, one of the very clear indicators of this transition point for the JICF is through observed changes in hotwire-based spectral contour plots of vertical velocity power spectra along the evolving shear layer trajectory. When the flow is CU, the contour plots depict relatively weak broadband instability peaks, frequency shifting along the trajectory due to a tonal interference with the hotwire probe (Hussain & Zaman 1978; Getsinger *et al.* 2012), and the formation of a subharmonic instability peak. When the flow becomes AU, the contour plots show a stronger and more pure-toned instability with higher harmonics which do

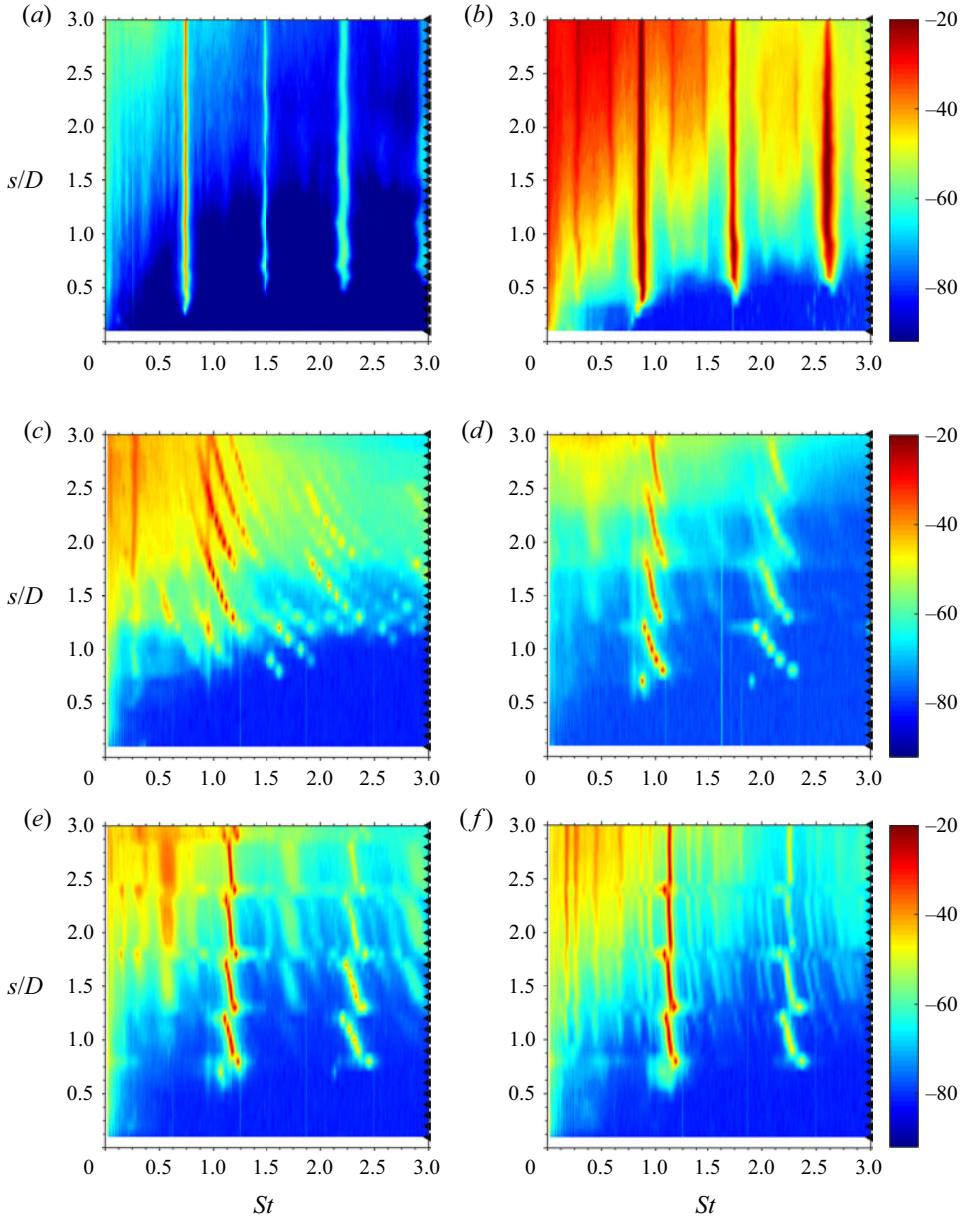

Figure 5. Upstream shear layer spectral contour maps of the spatial evolution of shear layer instabilities for an acetone seeded, equidensity, $Re_j = 2300$ jet at $J = 7$. (*a*) Original jet nozzle. (*b*) Non-tabbed extension. (*c*) Tab upstream. (*d*) Tab downstream. (*e*) Tab L90. (*f*) Tab R90.

not vary significantly along the shear layer, in addition to elimination of the subharmonic presence.

For an equidensity flush nozzle-injected jet with a jet Reynolds number of $Re_j = 2300$ and an acetone mole fraction of $\psi = 0.218$, the critical transition from convective to absolute instability takes place at $J_{cr} \approx 8$ (Shoji *et al.* 2020*b*). Representative spectral contour plots for hotwire data taken along the USL for the transverse jet with the original

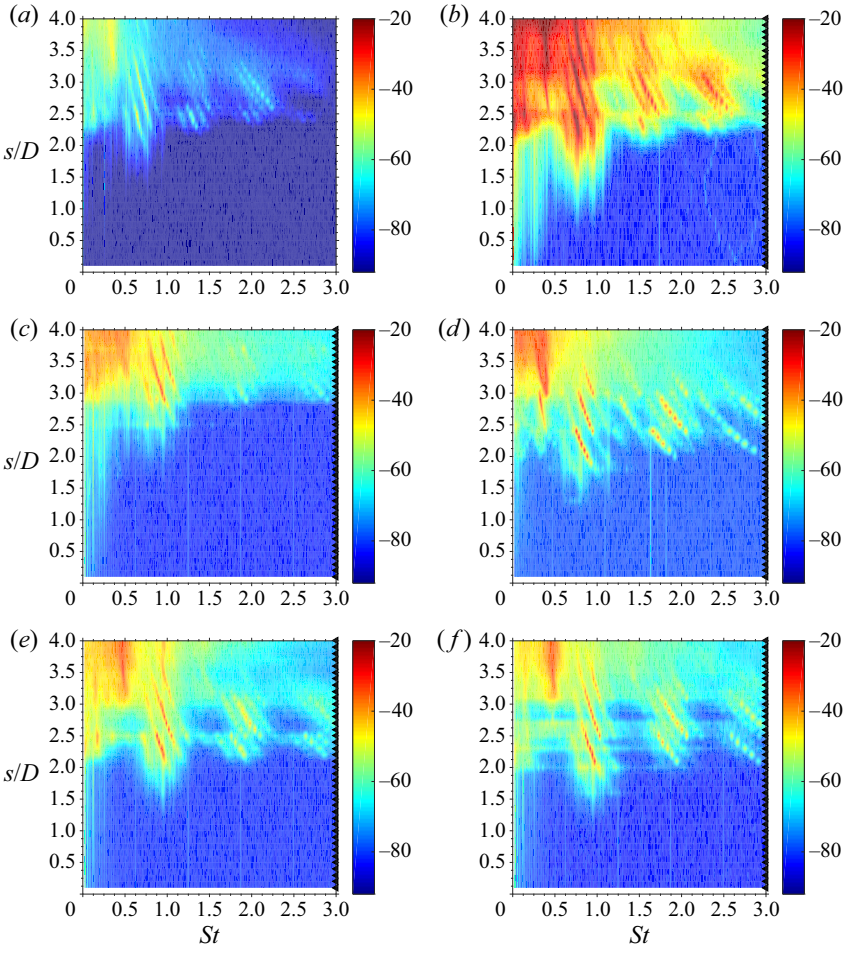

Figure 6. Upstream shear layer spectral contour maps of the spatial evolution of shear layer instabilities for an acetone seeded, equidensity, $Re_j = 2300$ jet at $J = 61$. (*a*) Original jet nozzle. (*b*) Non-tabbed extension. (*c*) Tab upstream. (*d*) Tab downstream. (*e*) Tab L90. (*f*) Tab R90.

fifth-order polynomial nozzle are shown in figure 5(*a*) for the case of an AU USL at $J = 7$, and in figure 6(*a*) for the case of a CU USL for $J = 61$. Along the abscissa, frequency content was non-dimensionalized to show a Strouhal number based on the jet diameter, $St \equiv fD/U_j$, while in the ordinate the shear layer trajectory location s was normalized by the jet exit diameter D. Strong pure-tone instability characteristics in figure 5(*a*) and delayed, weaker instabilites with frequency shifting, representing tonal interference, in figure 6(*a*) are consistent with AU and CU USL instabilities, respectively.

To explore the influence of the presence of a tab placed about the jet exit periphery on the USL instabilities, the tab insert was oriented at various positions relative to the upstream, including upstream and downstream locations, and resulting USL spectral characteristics for these cases are shown in figures 5(*c–f*) and 6(*c–f*). Because the tab extensions had a finite thickness, increasing the nozzle length by $0.19D$, it was also necessary to explore the effect of the simple round template without a tab, replacing the tab extension template, to examine that influence on USL instabilities. These results are shown in figures 5(*b*) and 6(*b*).

For the naturally AU cases at $J = 7$, the simple round (tabless) thin extension in figure 5(*b*) shows that the shear layer instabilities were only slightly altered as compared with the original flush nozzle. Here the shear layer instability was still strong and pure-toned, with only a very slight increase in the associated frequency of the dominant mode. These changes due to the nozzle extension were relatively small, and the resulting jet was certainly considered to be AU, but it did appear that the small straight extension at the nozzle end may have altered the upstream momentum thickness of the jet, hence affecting the dominant instability frequency (Alves *et al.* 2008). These alterations in the velocity field and momentum thickness are explored in simultaneous PLIF and PIV imaging experiments.

The presence of the physical tab in the extension to the nozzle for $J = 7$ had a much more significant influence on shear layer instabilities, in many cases. When the tab was situated at the upstream location (figure 5*c*), a significant change in the spectral characteristics took place, producing clear features of convective instability in the USL, with a delay in initiation of the instabilities and frequency shifting over a large span of frequencies. Unexpectedly a lower frequency peak was formed at $St = 0.32$, which did not correspond to the typical subharmonic of the fundamental range ($St_0 \approx 1.1$–1.5), as is typically observed for CU conditions in Megerian *et al.* (2007). Interestingly, a Strouhal number of 0.32 is in the range of established values of preferred modes for the free jet emanating from a nozzle (Gutmark & Ho 1983; Petersen & Samet 1988), but at much higher jet Reynolds numbers, of the order 10^5. This difference in dominant subharmonic frequencies would be consistent with alterations of the jet momentum thickness, recalling from linear stability theory that as D/θ changes, so do the growth rate curves of the instabilities, and, thus, the dominant instability frequency (Alves *et al.* 2008). Remarkably, when the tab was placed in the downstream shear layer (figure 5*d*), the resulting instability characteristics in the USL were similarly representative of a convective instability, with a delay in initiation and persistent frequency shifting typical of tonal interference for a CU USL. When the tab was oriented at the L90 and R90 positions (figures 5*e* and 5*f*, respectively), the USL instabilities were only slightly weakened as compared with the instabilities for the non-tabbed case in figure 5(*b*), with a slight frequency shifting for the entire three diameters along the shear layer. In the L90 tab orientation there was also clear emergence of a subharmonic instability, but this was not the case for R90, and even less so for the downstream tab positioning in figure 5(*d*). These factors suggested that the presence of the tab transitioned the USL for $J = 7$ from being AU without the tab to CU or nearly so with the tab, especially when situated in the upstream region of the jet exit.

The influence of the non-tabbed and tabbed inserts on USL instability characteristics for the naturally CU flow at $J = 61$ is shown in figure 6(*b–f*). Similar to the naturally AU case in figure 5(*b*), the simple round thin extension to the nozzle produced spectral characteristics which were very similar to the original jet without any extension (figure 6*a*), with a slight increase in the average of the dominant frequency. Note that the tonal interference characteristic of the JICF with a CU USL was clearly evident in both figures 6(*b*) and 6(*a*). We note that the instability strengths shown in the colour maps in figure 6(*b*) as well as figure 5(*b*) were slightly altered from other cases due to minor differences in the method for extracting spectra. For the $J = 61$ cases with a tab partially blocking the jet flow, when the tab was oriented at the downstream position (figure 6*d*), or at L90 or R90 (figure 6*e* or 6*f*, respectively), the resulting instability characteristics were very similar to the original jet configuration. When the tab was oriented at the upstream region of the jet (figure 6*c*), however, a rather significant alteration to the instabilities along the shear layer trajectory took place, where the initiation of the instability was delayed nearly to a distance of $s/D \approx 3$ along the shear layer, in contrast to the initiation location

of $s/D < 2$ without the tabless insert in figure 6(a). This delay in the onset of the shear layer instabilities not only suggested a weakening of the disturbance, but also indicated spectral characteristics at a high J value that were similar to those for a free jet or transverse jet emanating from a pipe rather than a nozzle, as seen by Getsinger *et al.* (2014). This observation also would be consistent with an increase in the momentum thickness in the upstream region of the jet due to the presence of a tab. Situating the tab upstream appeared to alter the subharmonic formation and shear layer rollup, producing weaker and more diffuse or broadband energy transfer to the subharmonics from the fundamental instability.

Hence, in both naturally AU and CU JICF conditions, the most significant influence of the tab on the USL was, as would be expected, when it was positioned within the USL. Yet it is interesting that the USL for $J = 7$ was also influenced by tab positioning away from the upstream, even at the downstream location, in contrast to a lack of significant influence for such tab positions on the naturally CU case of $J = 61$. These behaviours in fact agree with the computationally predicted wavemaker regions of both convectively and AU low speed jets in crossflow, that is, the regions of greatest sensitivity to perturbations within the flow field (Regan & Mahesh 2019). These DNS indicate that a naturally AU transverse jet has a wavemaker region in the upstream near-field region of the jet, whereas the wavemaker region for a naturally CU JICF extends along the entire USL of the jet and wraps around to the downstream side of the jet. This similarity between experiments and simulations will be discussed in greater detail with regard to the structural changes in the following section.

3.2. *Structural characteristics*

The structural characteristics of the tabbed jet in crossflow were explored through instantaneous centreplane and mean cross-section PLIF images. Representative PLIF images are shown in figure 7 for the case of $J = 7$ and in figure 8 for the JICF with $J = 61$. The colour bars for the images represent the relative concentration of jet fluid scaled from 0 for pure crossflow to 1 for pure jet fluid, as was found in the potential core visible in the centreplane images. Cross-sectional concentration values were calibrated by a comparison of the spatially averaged cross-sectional concentration with that in a thin slice of a mean centreplane image, as described in Gevorkyan *et al.* (2016). Hence, the upper limit of the concentration scales corresponded to the maximum value within each individual image. Cross-sectional images represent an average of 500 instantaneous snapshots of the flow field, and in the experiments were taken at x/D locations of 2.5, 5.5 and 10.5 downstream of the jet injection. In figures 7 and 8 only cross-sectional images corresponding to $x/d = 10.5$ are shown since they depict the more developed and visually obvious implications of tabs on the jet structure. The overall study (Harris 2020) investigated additional J values and tab orientations. The results shown here deal primarily with the conditions examined in the preceding § 3.1. In addition to the non-tabbed thin insert and upstream, downstream and L90/R90 tab positioning, results are also shown for a few tab orientations between the upstream and L90/R90 locations.

The instantaneous centreplane and mean cross-sectional images for $J = 7$ in figure 7 show that the jets were similar to one another in terms of overall spread and penetration in the centreplane and relative cross-sectional symmetry, though there were some subtle differences in each. In the instantaneous centreplane images in figure 6(a), one sees clear USL vortex rollup for the non-tabbed jet with the thin extension, consistent with the pure-tone instability observed in figure 5(b). But with the tab in the upstream position, the weakening in the USL as indicated in figure 5(c) was manifested in a weakening and

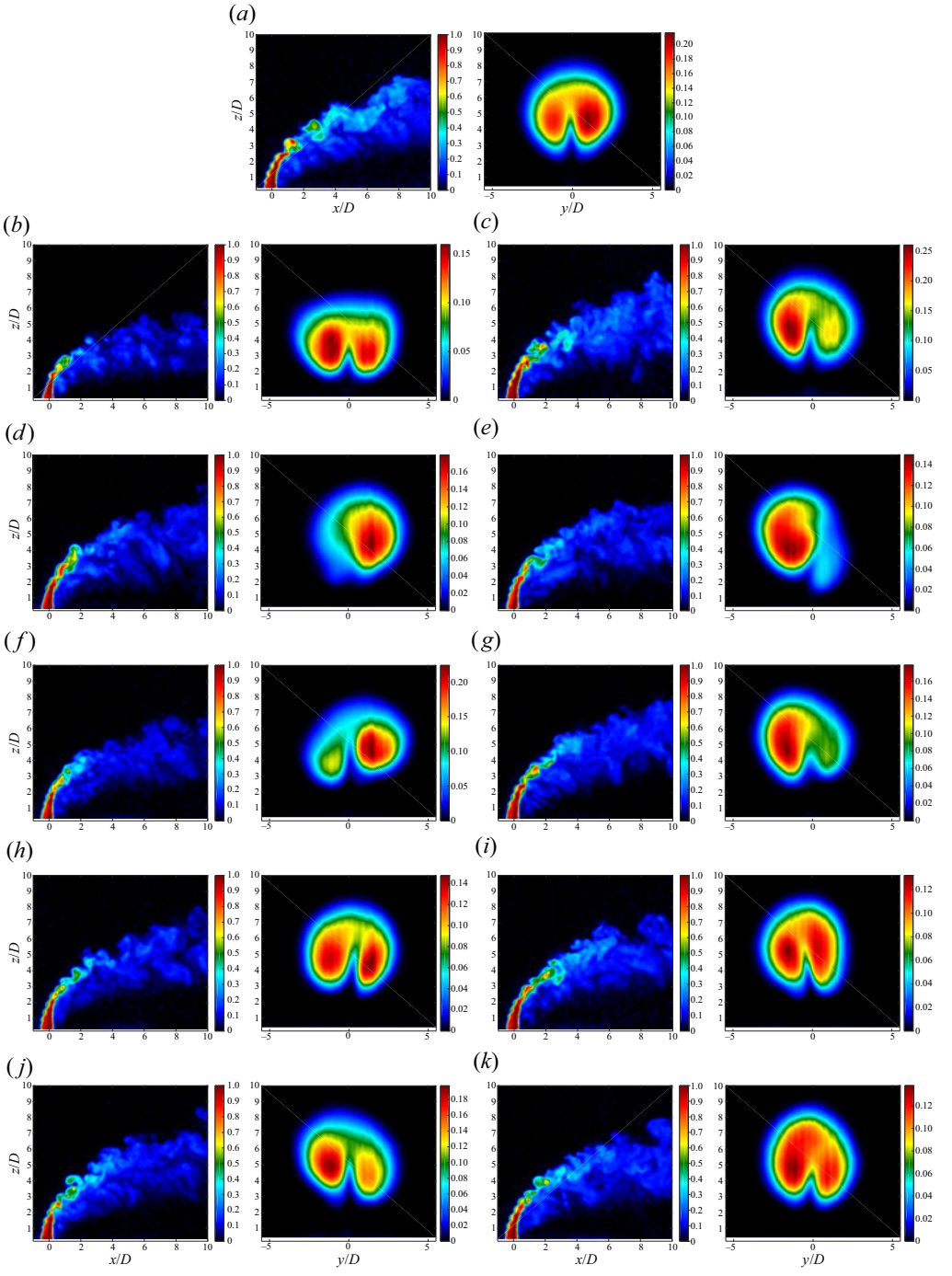

Figure 7. Structural characteristics for the JICF at $J = 7$ and $Re_j = 2300$. Shown for each condition is an instantaneous centreplane image and mean cross-sectional PLIF image at $x/D = 10.5$. (*a*) Non-tabbed extension. (*b*) Tab upstream. (*c*) Tab downstream. (*d*) Tab L30. (*e*) Tab R30. (*f*) Tab L45. (*g*) Tab R45. (*h*) Tab L60. (*i*) Tab R60. (*j*) Tab L90. (*k*) Tab R90.

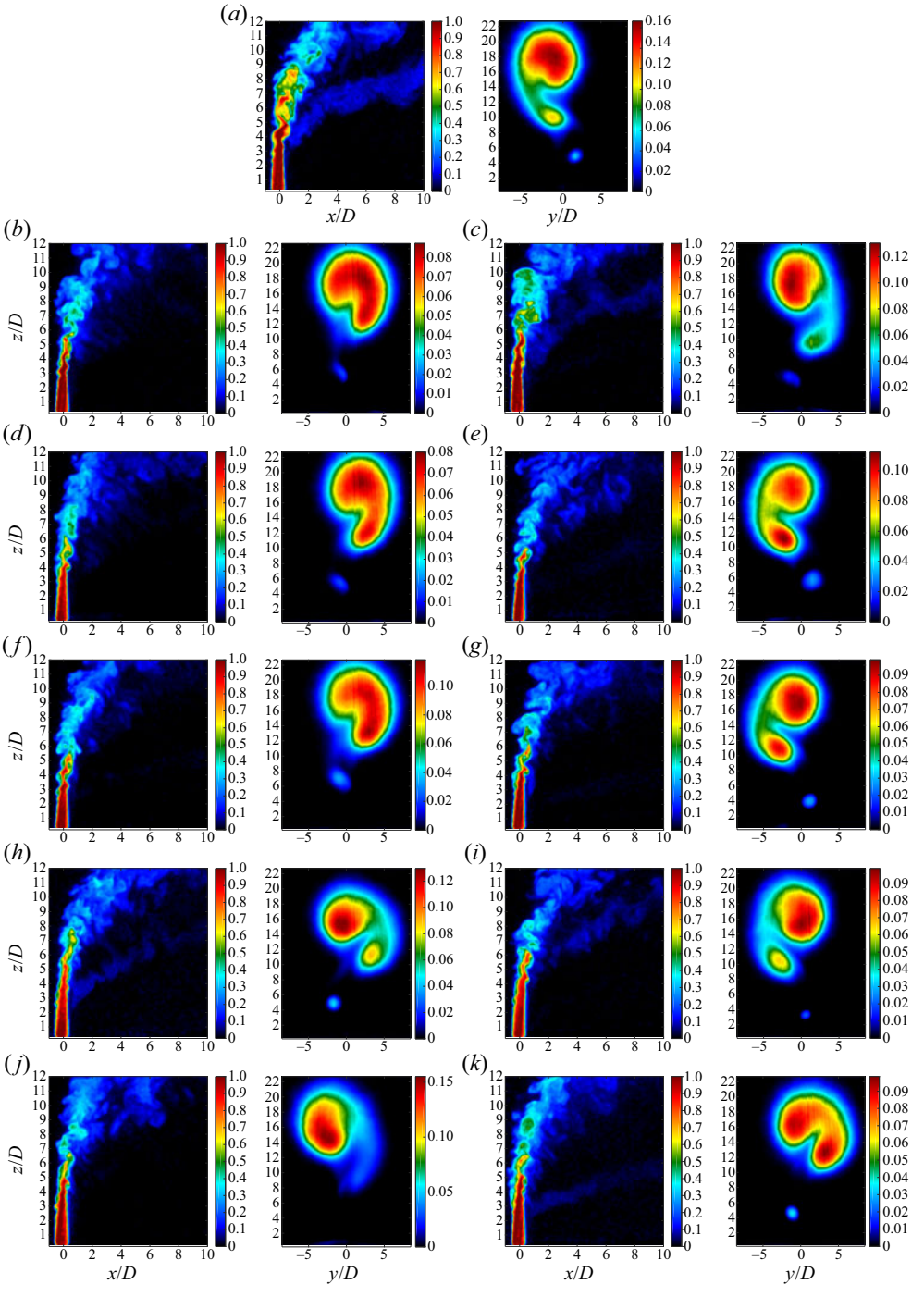

Figure 8. Structural characteristics for the JICF at $J = 61$ and $Re_j = 2300$. Shown for each condition is an instantaneous centreplane image and mean cross-sectional PLIF image at $x/D = 10.5$. (*a*) Non-tabbed extension. (*b*) Tab upstream. (*c*) Tab downstream. (*d*) Tab L15. (*e*) Tab R15. (*f*) Tab L30. (*g*) Tab R30. (*h*) Tab L60. (*i*) Tab R60. (*j*) Tab L90.(*k*) Tab R90.

smoothed upstream edge of the USL. This weakening was observed in other centreplane images with tabs placed close to the upstream region, e.g. at R30 or L45. For such cases there was also a small but discernible decrease in the penetration of the jet into the crossflow, especially for upstream tab placement. Such observations on penetration have been seen in prior studies of the tabbed jet in crossflow when a tab is placed upstream (Liscinsky *et al.* 1995; Zaman & Foss 1997; Bunyajitradulya & Sathapornnanon 2005). These studies suggest the decrease in penetration arises due to the conflicting signs of vorticity generation from the tab and counter-rotating bound vortex pair. Cross-sectional imaging here can help to explore this conjecture.

The cross-sectional images in figure 7 show the classic symmetric CVP structure for the non-tabbed jet with a thin extension (figure 7*a*), but when the tab was placed upstream (figure 7*b*), the weakened USL had the effect of flattening the CVP structure, though it retained the same general CVP-like shape. Other tab locations in which there was a smoothing/weakening of the USL vortices produced cross-sectional structures that were actually asymmetric and, in fact, did not appear to create a CVP, such as the cases where tabs were placed at L30, R30 or R45. In other instances the CVP structure became tilted or asymmetric as a result of the tab. Thus, USL vortex rollup and CVP symmetry appeared to be linked, consistent with the more significant effect of the tab on USL instabilities in spectral plots for $J = 7$ (figure 5) as well as ideas on the formation of the CVP from three-dimensional vortex simulations (Cortelezzi & Karagozian 2001). For the asymmetric jet cross-section, the bulk of the jet fluid was aligned opposite to or deflected away from that of the tab position. The asymmetries generated agreed with the findings of Bunyajitradulya & Sathapornnanon (2005), who note asymmetric structures arising from azimuthal placement of the tab away from the upstream of the jet. Also in agreement with this prior study, we observed a decrease in the severity of CVP alteration as the tab was moved further from the upstream region of the jet, where tab positions past L60/R60, towards the downstream region of the jet, showed few perceptible differences in the cross-section and centreplane as compared with the non-tabbed case. These findings on the sensitivity of tab placement to its proximity to the upstream region also were consistent with the proposed wavemaker region of an AU JICF from adjoint sensitivity analysis of the DNS by Regan & Mahesh (2019), incorporated the same geometry as in the original nozzle in our experiments.

While the USL spectral alterations for the naturally AU $J = 7$ transverse jet were rather significant (figure 5) and the centreplane-based and cross-section-based PLIF images showed corresponding alterations consistent with these spectral changes (figure 7), when the momentum flux ratio was increased from $J = 7$ to $J = 61$, as shown in figure 8, PLIF images showed much more dramatic alterations than expected from the relatively minimal spectral changes shown in figure 6. For the non-tabbed thin round template (figure 8*a*), the mean cross-section at $x/D = 10.5$ showed a highly asymmetric structure, forming a type of reverse question mark shape with a small tertiary vortical structure, as observed in earlier studies for the original nozzle-generated JICF at a high momentum flux ratio. Under these conditions the jet has a relatively weak CU USL, and as a result it is susceptible to perturbations or imperfections in the incoming flow (Getsinger *et al.* 2014). These earlier studies explore alternative injection arrangements with the same flush nozzle as well as small alterations in the incoming crossflow to attempt to alter this asymmetry, yet the asymmetry persists and remains highly repeatable to within the present experimental capabilities. Such natural asymmetries are consistent with earlier linear stability analyses suggesting that growth rates for natural helical instability modes for the JICF at larger

momentum flux ratios J have different positive and negative values (Alves *et al.* 2007), and, thus, could be associated with asymmetry in the flow.

With the presence of small tabs for $J = 61$, as was seen for the jet at $J = 7$, figure 8 indicates that placement of the tab upstream had the most profound impact on the issuing jet, consistent with the rather substantial alteration to spectral characteristics created by the upstream tab, shown in figure 6(*c*). As indicated in figure 8(*b*), the tertiary flow structure was generally weakened or eliminated, and the cross-section appeared to flip in its asymmetric orientation. Among all of the tab placements for $J = 61$, the upstream positioning caused the cross-section to become more symmetric, closer to the classical CVP structure and potentially affecting the jet's molecular mixing (Gevorkyan *et al.* 2016), as will be discussed in the next section. As the tab orientation was rotated away from the upstream location azimuthally towards the downstream, the jet was seen to bulk deflect away from the tab. While this is noted for $J = 7$ to a limited degree, the alteration in cross-section with tabs for this higher J condition was quite dramatic, with complete flipping of the asymmetric structure from one side to the other, depending on tab placement. Tabs placed to the left or the right side of the jet orifice by the same angle appeared to create cross-sections that were reversed (though not precisely mirrored) images of one another between 15 and 60°. This was not observed as clearly for tabs at 90° nor at the downstream position however. Overall, such observations are remarkable in that the effects of the tabs on the localized USL instabilities, indicated in figure 6, were rather minimal, except for upstream placement, yet the effect of tabs on the jet cross-sectional shape was quite significant in most cases. Further, unlike the $J = 7$ cases, the influence of the tab at $J = 61$ remained quite impactful well past the R60 or L60 orientations, where the R90, L90 and tab downstream configurations all produced changes in the cross-sectional structure of the jet. The more significant influence of tabs even at L90 and R90 for this larger J value was similar to observations by Zaman & Milanovic (2012), who studied the influence of oscillating tabs at the same locations. At $J = 48$, these researchers see a significant impact of such oscillating tabs on jet cross-sectional structure, but for $J < 15$, there is little jet response, somewhat similar to our relatively minimal $J = 7$ structural impacts in figure 7, though it is noted that the studies in Zaman & Milanovic (2012) were at much larger Reynolds numbers. While our findings cannot be explained by USL spectral changes alone, they are supported by the proposed wavemaker region of a CU JICF. Adjoint sensitivity analysis of the DNS by Regan & Mahesh (2019) for a JICF with $J = 16$ indicates that the wavemaker extends along the entire USL of the jet, and even wraps around towards the downstream side of the jet as the flow is deflected and reoriented with the crossflow. In light of this, it may be that the wavemaker region continues to grow around the periphery of the jet nozzle exit as the momentum flux ratio is increased until the downstream side of the jet is enveloped. Irrespective of the origins of the jet behaviour at such conditions, the alterations to the structural characteristics with the tab placed beyond the upstream region were quite remarkable, as they depict the first documented alteration of the JICF under such conditions due to such a tab placement. All prior studies of the fixed tabbed JICF theorize that the tab downstream would have the greatest impact upon the flow, but instead they find that placement to have no significant influence (Liscinsky *et al.* 1995; Zaman 1998; Bunyajitradulya & Sathapornnanon 2005). Yet it should be noted that these prior studies explore the JICF at much higher jet Reynolds numbers than in the current study, with symmetric cross-sectional flow structures in the absence of the tab. Clearly, further exploration of the influence of the tab on jet dynamics and structure for a range of jet Reynolds numbers and potentially for different injector configurations would help to illuminate the reasons for these differences.

3.3. *Mixing characteristics*

Quantification of the molecular mixing between the jet and crossflow was explored via the unmixedness parameter, which as noted earlier represents the second moment of the scalar concentration field, and can be derived from the high-resolution PLIF images. The equation defining unmixedness in the jet cross-section is shown in (2.1), where the lower the local unmixedness, U, the better the molecular mixing. The unmixedness was calculated from centreplane and cross-sectional views of the jet, where the former provided a continuous downstream evolution of the jet mixing, and the latter provided a more complete picture of the local mixing for a particular downstream location. In either approach, the general mixing trends as the jet evolves have been shown to be generally in agreement with one another (Gevorkyan *et al.* 2016). The conditions presented in the plots which follow depict every tab orientation tested, consisting of the non-tabbed round thin extension and cases with the tab upstream, tab downstream and with tab orientations at every 15° azimuthally from the upstream to the L90 and R90 locations.

Figure 9 shows plots representing the centreplane and cross-sectional mixing of the $J = 7$ jet, where the results are separated such that all of the left oriented tab locations appear in one plot, and all of the right oriented locations appear in another, with the non-tabbed, tab upstream and tab downstream appearing in both for comparative purposes. Unmixedness determined from the cross-sectional imaging is shown at the three locations explored, $x/D = 2.5, 5.5$ and 10.5. Among the least effective mixing configurations (highest U) were the cases with the non-tabbed simple extension and the downstream tab, and these were consistent for both centreline-based and cross-section-based unmixedness. This finding was consistent with the ineffectiveness of the downstream tab in improving JICF mixing documented in experimental studies by Liscinsky *et al.* (1995). The apparent worsening of the downstream tab's mixing as compared with the non-tabbed case in figure 9 may be linked to the transition of the USL instabilities from AU to CU, seen in figure 5(*d*), with an associated asymmetry in the jet cross-section (figure 7*c*). This correlation among the state of the USL instability, cross-sectional structure and molecular mixing are known to exist for the unforced, original nozzle-based JICF studied in Gevorkyan *et al.* (2016).

Yet interestingly, the mixing results in figure 9 also suggested that the tab upstream orientation, which introduced an even more significant weakening of the USL from AU to CU, and a flattened (yet still symmetric) cross-sectional CVP structure, appeared to be the best mixer, with a remarkable improvement in molecular mixedness over that of the non-tabbed jet. This behaviour was documented in both the centreplane and cross-sectional views. Hence, the weakened USL instability here was not as significant to the mixing alteration, likely because the cross-section remained mostly CVP-like, potentially with improved local entrainment of crossflow. It is also noted that the thicker USL at injection created by the upstream tab was reminiscent of a thicker USL created by a pipe rather than a nozzle, as explored in prior studies. Getsinger *et al.* (2014) noted that for the same flow conditions as explored in this study, for $J = 7$, an AU jet producing a fully developed pipe flow has a more diffuse, flattened CVP structure and, per the quantification in Gevorkyan *et al.* (2016), it tends to be a better mixer than the AU jet issuing with a top hat velocity profile from a nozzle, especially further downstream. The initial USL differences here could be the relevant factor in structural and mixing enhancement by an upstream-oriented tab.

In examining other tab orientations, the L45 and R15 cases also appeared to be excellent mixers per the centreplane mixing quantifications, matching the unmixedness values of the tab upstream case. The fact that different tab angles between the left and right orientations produced more optimal mixing was likely attributable to the centreplane's representing a

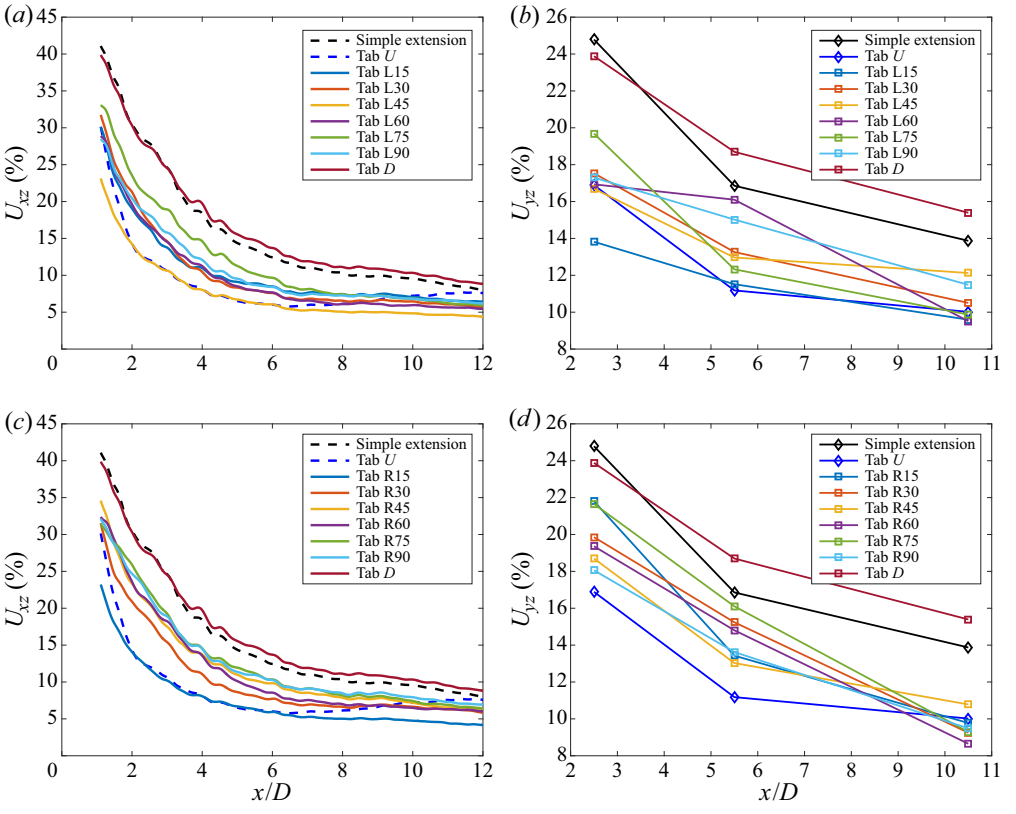

Figure 9. Downstream evolution of centreplane unmixedness U_{xz} and cross-section-based unmixedness U_{yz} for $J = 7$ and $Re_j = 2300$, for the non-tabbed case and various tab orientations about the jet periphery. (*a*) Centreplane unmixedness (left tabs). (*b*) Cross-sectional unmixedness (left tabs). (*c*) Centreplane unmixedness (right tabs). (*d*) Cross-sectional unmixedness (right tabs).

very thin slice of the jet, and indeed, when looking in the cross-section, the trends were slightly different. For cross-sectional mixing quantification, the L15 and R90 appeared to be the next best mixers following the upstream tab configuration. These findings for $J = 7$ jets with a tab suggested that while there can be improvements to the mixing of the jet due to the presence of a tab, optimal tab orientation may be more difficult to establish, due in part to the asymmetric jet structure for which there can be relatively small differences in mixing statistics. Regardless, it is clear that qualitative trends showed as the tab orientation was shifted from the upstream towards the downstream, the improvement in mixing was systematically reduced.

A similar presentation of mixing characteristics for the naturally CU case with $J = 61$ is shown in figure 10. Notably, and in contrast to the $J = 7$ results, positioning of the tab downstream actually improved the molecular mixing as compared with the non-tabbed jet. Despite it not altering the jet shear layer instabilities (figure 6*d*), the tab downstream was able to impact the structural characteristics (figure 8*c*), and in fact caused the asymmetry in the jet cross-section to completely reverse, though the tertiary vortex structure for the downstream case was weaker than for the original (non-tabbed) jet. For the configuration with the tab upstream, while the USL instability was weakened and delayed compared with the non-tabbed jet (figure 6*c*), structurally a somewhat more symmetric jet was produced, per figure 8(*b*), and correspondingly figure 10 shows that configuration improved mixing to

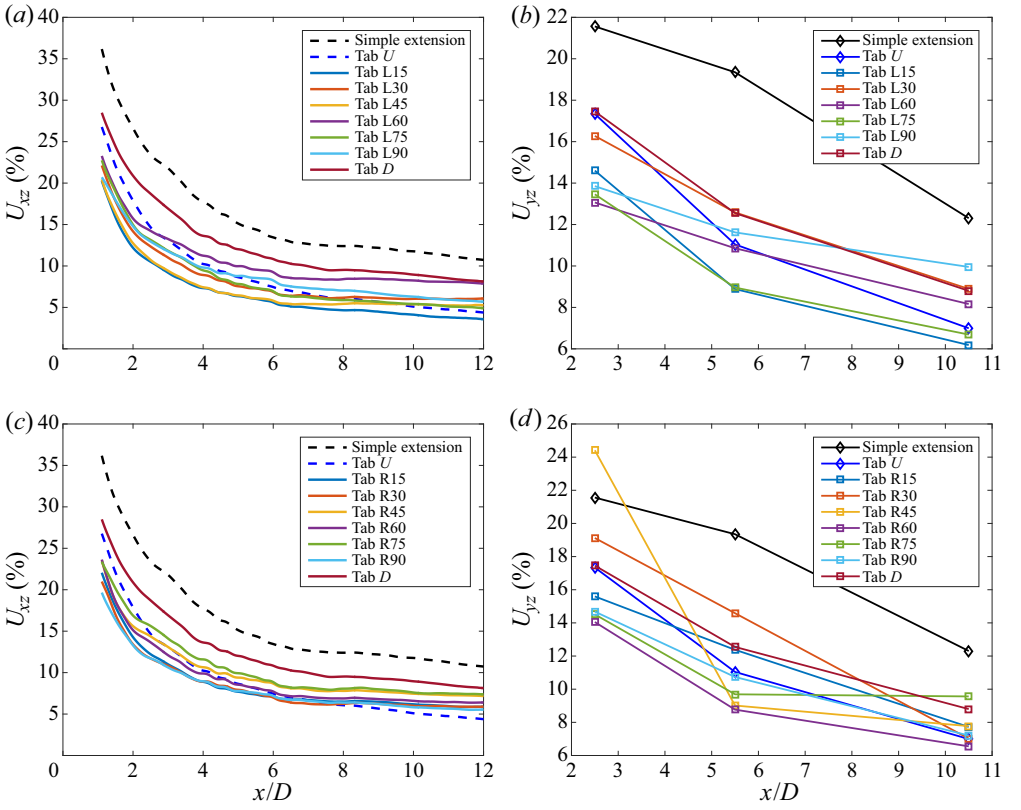

Figure 10. Downstream evolution of centreplane unmixedness U_{xz} and cross-section-based unmixedness U_{yz} for $J = 61$ and $Re_j = 2300$, for the non-tabbed case and various tab orientations about the jet periphery. (*a*) Centreplane unmixedness (left tabs). (*b*) Cross-sectional unmixedness (left tabs). (*c*) Centreplane unmixedness (right tabs). (*d*) Cross-sectional unmixedness (right tabs).

a significant degree. Even other tab orientations for which cross-sectional flow structures remained quite asymmetric still improved the molecular mixing of the jet over that of the tabless jet, e.g. for L90 or R45. The marked improvement in centreplane mixing, almost irrespective of tab orientation in figure 10, may speak to the relative weakness of the crossflow and the shear layer instabilities surrounding the jet, and, hence, the susceptibility to disturbances introduced through the tabs. If applied appropriately, such passive disturbances as tabs can produce rather significant improvements in mixing, as demonstrated in figures 9 and 10.

3.4. *Centreplane and cross-sectional vorticity*

The present experiments also explored the influence of tabs on near-field vorticity and shear layer dynamics via simultaneous PLIF and PIV imaging. For these simultaneous PLIF and PIV imaging experiments, the jet flow conditions were changed from an acetone mole fraction of $\psi = 0.218$, jet bulk velocity of $U_j = 7.91$ m s^{-1} and jet Reynolds number of $Re_j = 2300$, to values of $\psi = 0.112$, $U_j = 6.80$ m s^{-1} and $Re_j = 1900$. To determine the effect of these differences in flow conditions, the structural and mixing characteristics of both flow fields, for a variety of momentum flux ratios, were compared and are detailed in Harris (2020). This was done not only to demonstrate the similarity in tab effects for a

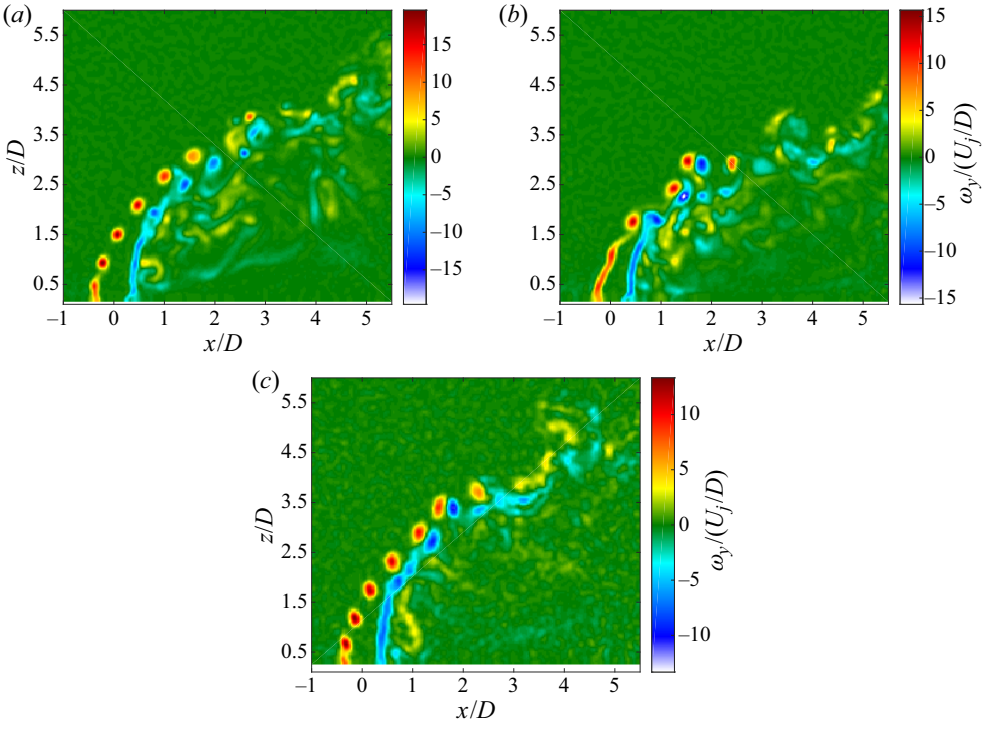

Figure 11. Centreplane images of the scaled instantaneous vorticity field for the AU jet at $J = 5$ and $Re_j = 1900$. The colourbars are scaled to the same maximum and minimum vorticity values contained within all images shown. (*a*) Simple non-tabbed extension. (*b*) Tab upstream. (*c*) Tab downstream.

given state of the USL, but also to verify the usefulness of even a lesser degree of PLIF resolution in extracting overall trends in mixing metrics. It was found that there was good agreement in terms of instability characteristics and mixing trends between the different sets of jet flows for momentum flux ratios with similarly absolutely or CU USL instability characteristics.

It was of interest in the PIV-based experiments to quantify the vorticity field in both the centreplane (x–z) and cross-sectional plane (y–z). The early work of Zaman & Foss (1997) and Zaman (1998) suggests that upstream and downstream tab placements are ineffective due to the generation of vorticity opposite to the CVP in the case of the former, and the pressure gradient in the wake of the jet in the case of the latter. It is noted that these experiments are performed at fairly large momentum flux ratios, however, exceeding $J = 21$. The high-resolution PLIF imaging of the tabbed JICF demonstrates that both upstream- and downstream-positioned tabs can influence jet cross-sectional structure and mixing, depending on the flow regime and the nature of the USL in the absence of tabs. Understanding the vorticity evolution in this flow field can thus assist in interpreting other flow features, especially those related to the dynamics of the USL and its role in CVP structure.

Figure 11 shows instantaneous snapshots of vorticity along the centreplane of the JICF at a momentum flux ratio of $J = 5$ for the non-tabbed jet (with the thin round template extension), the tab positioned upstream and the tab downstream. Corresponding mean cross-sectional vorticity images for the same flow and jet geometrical configurations as in figure 11 are shown in figure 12, with images provided at three different downstream

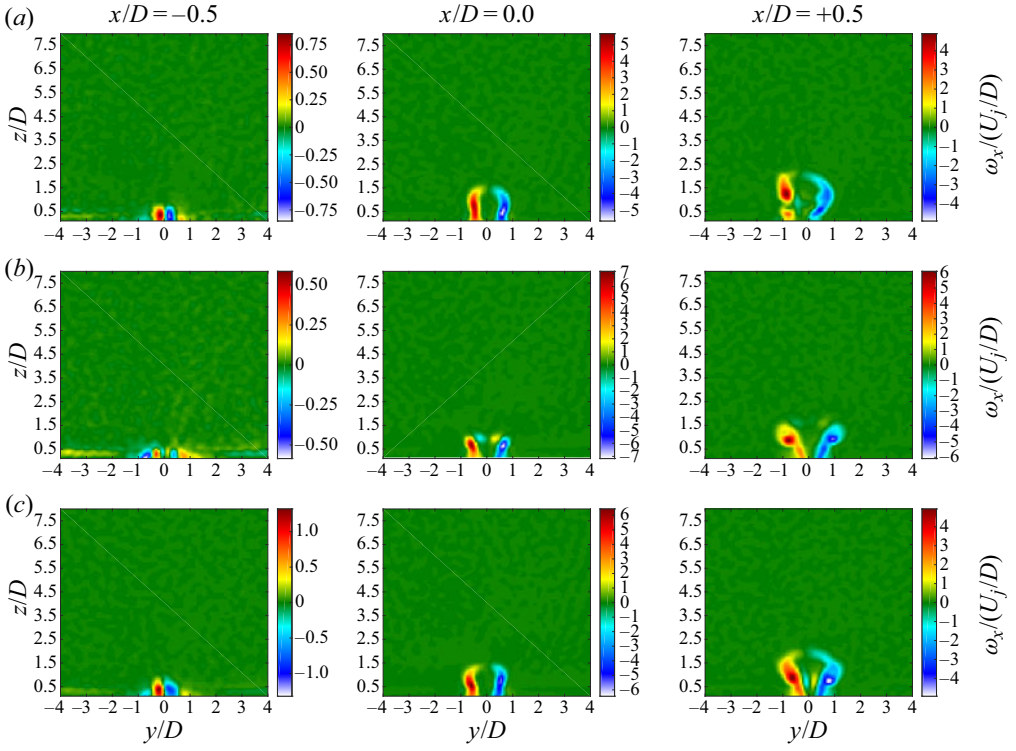

Figure 12. Mean cross-sectional vorticity images at cross-sectional locations $x/D = -0.5$, $x/D = 0.0$ and $x/D = +0.5$. Images correspond to the (*a*) non-tabbed jet, (*b*) tab upstream jet and (*c*) tab downstream jet, with $J = 5$ and $Re_j = 1900$. The colourbars are scaled to the maximum and minimum vorticity values contained within each image shown.

locations corresponding to the upstream leading edge of the jet exit ($x/D = -0.5$), the centre of the jet exit ($x/D = 0.0$) and the downstream trailing edge of the jet exit ($x/D = +0.5$). Averaging in these and subsequent mean vorticity images was performed over 500 realizations. For the instantaneous centreplane vorticity without a tab (figure 11*a*), USL vortex rollup initiated very close to the jet exit, at approximately 0.5 diameters, while the downstream vorticity did not begin to pinch-off until almost 1 diameter after pinch-off in the USL. This vorticity evolution was consistent with that for an AU/GU USL for the nozzle-generated jet in the absence of the thin extension in earlier studies (Gevorkyan *et al.* 2018), including vorticity magnitude and shear layer instability differences between the windward and leeside of the jet (Davitian *et al.* 2010*a*; Regan & Mahesh 2017). The mean cross-sectional vorticity evolution of the jet at three different locations at or near the jet exit in figure 12(*a*) showed that, in general, the vorticity initiation was relatively symmetric at the upstream edge ($x/D = -0.5$) and at the centre of the jet ($x/D = 0.0$) for the jet without a physical tab. The vorticity at the downstream edge of the jet exit, at $x/D = +0.5$, was slightly asymmetric for the tabless jet, interestingly. This overall behaviour in figure 12(*a*) was not unexpected given that the USL is naturally AU at $J = 5$ for this jet mixture (Shoji *et al.* 2020*b*), and growth of asymmetries is shown to be suppressed by the larger dominant axisymmetric USL instability mode (Alves *et al.* 2007; Regan & Mahesh 2017), resulting in symmetric CVP structures at low J values (Getsinger *et al.* 2014).

When a tab was placed in the upstream edge of the jet at $J = 5$, the centreplane instantaneous vorticity image (figure 11*b*) showed the upstream vorticity initiation to be

delayed by 0.50–0.75 diameters, and the overall magnitude of the vorticity in this plane to be significantly weakened as compared with the characteristics shown for the non-tabbed jet (figure 11*a*). These observations were consistent with the observed delay and significant weakening of USL instabilities for the naturally AU jet at $J = 7$ in the high-resolution PLIF results with an upstream tab. Interestingly, in figure 11(*b*) the upstream tab caused the downstream vorticity dynamics to have approximately the same vortex pinch-off location as for the non-tabbed jet, as well as a slight increase in the maximum downstream vorticity. This may be interpreted by examining the cross-sectional vorticity evolution (figure 12*b*), where the tab upstream significantly weakened the vorticity generation along the windward side of the jet, shown (as expected) by the vorticity magnitudes at $x/D = -0.5$. But as the jet evolved to the cross-sectional locations $x/D = 0.0$ and $+0.5$, the vorticity actually became slightly stronger than for the non-tabbed jet. The apparent net result of the tab upstream was a dampening of the vorticity generation directly in the upstream region, yet a small but notable increase in vorticity production along the sides and downstream edge of the jet. Though in principle the net vorticity generation from a tab upstream should reorient and act to cancel or at least weaken the CVP, the strengthening of vorticity generation in the downstream region actually created a greater symmetry in the downstream vorticity field and, hence, produced contributions to a symmetric CVP. These observations on the upstream tab were consistent with earlier findings by Zaman (1998), who found that while the overall circulation from the vorticity isocontours may be lower with the tab upstream, the counter-rotating vortex pair still produces almost identical magnitudes of vorticity at the vortex cores to those for non-tabbed jets. These observations in figure 12(*b*) were also consistent with and help to explain the high-resolution PLIF-based cross-sectional jet structures for the case in figure 7(*b*) with an upstream tab at $J = 7$. In this case the CVP becomes only slightly flattened in comparison to the usual symmetric CVP for the non-tabbed transverse jet.

For a transverse jet with a tab placed at the downstream edge of the orifice, both Liscinsky *et al.* (1995) and Zaman & Foss (1997) found no difference in the overall vorticity and mixing dynamics compared with the non-tabbed jet, although as noted earlier, their experiments are performed at fairly large momentum flux ratios, exceeding $J = 21$. For a lower momentum flux ratio of $J = 7$ in the high-resolution PLIF experiments, the downstream tab caused the USL to become significantly weaker, as indicated in figure 5(*d*), transitioning from an absolute instability to a convective instability, although the degree of weakening in the USL was not as significant as that produced by an upstream tab. In the PIV-based vorticity measurements, figure 11(*c*) indicates that, while the vortex rollup along both the upstream and downstream sides of the jet initiated at nearly the same locations as the non-tabbed jet, the magnitudes of vorticity from both sides of the jet were significantly weakened, consistent with the weakening of the instability characteristics in figure 5(*d*). The cross-sectional vorticity magnitudes at various downstream locations in figure 12(*c*) also showed that a downstream tab produced nearly the same overall magnitude of vorticity as that is generated for the non-tabbed jet, and in fact for the most evolved view of the jet at $x/D = +0.5$, the vorticity production was more symmetric than for the non-tabbed jet, though not quite as symmetric as for the upstream tab. Thus, while vorticity directly in the upstream and downstream shear layers was weakened by the downstream tab, the overall vorticity produced in the sides of the jet remained relatively unchanged, leading to the relatively symmetric CVP structure observed far downstream for the case of $J = 7$ in figure 7(*c*). Hence, there was consistency in the near-field vorticity generation for both centreplane and cross-sectional planes with jet cross-sectional shape in the low J regime.

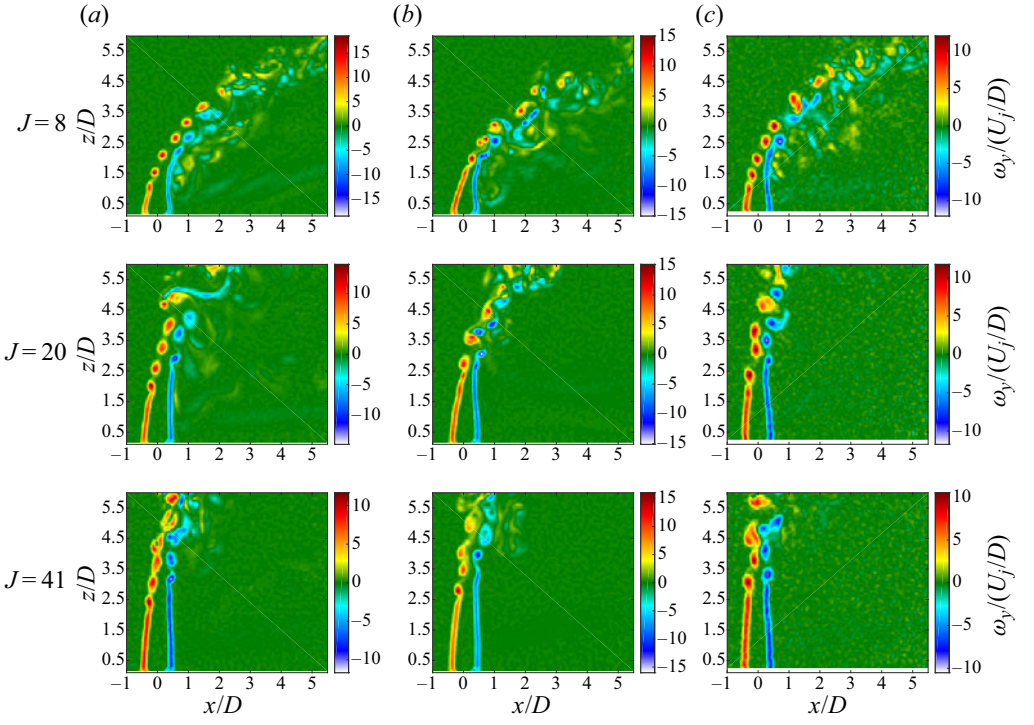

Figure 13. Centreplane images of the instantaneous vorticity field for the AU jet near the critical transition at $J = 8$ and CU jets at $J = 20$ and $J = 41$, all with $Re_j = 1900$. The colourbars are scaled to the maximum and minimum vorticity values contained within each image shown. (*a*) Simple extension. (*b*) Tab upstream. (*c*) Tab downstream.

Figure 13 shows representative instantaneous vorticity fields in the centreplane for larger values of J (8, 20 and 41) for the non-tabbed JICF with a thin extension, as well as for cases with the tab placed upstream and downstream. Figure 14 contains corresponding cross-sectional mean vorticity images at a downstream location $x/D = +0.5$ for these same flow and jet geometrical conditions. This location tended to produce the greatest differences among the different jet configurations. Instantaneous centreplane vorticity images in figure 13 suggested that for each jet configuration, with or without tabs, as the crossflow velocity was reduced (in order to increase J), upstream and downstream shear layer rollup was delayed further along the layer, consistent with earlier findings for the round JICF in Getsinger *et al.* (2014) and Gevorkyan *et al.* (2018). The upstream tab caused a further delay in the USL vorticity rollup as compared with the non-tabbed case, but for the tab placed downstream at higher J values there was relatively little change, similar to the case for $J = 5$ in figure 11. The magnitudes in figure 13 showed that both upstream and downstream shear layers had a stronger degree of vorticity generation for the non-tabbed case than for either case with tabs.

Cross-sectional mean vorticity fields for the three different configurations, shown for $J = 8$, 20 and 41 in figure 14, indicated that the degree of asymmetry for the non-tabbed jet increased for larger J values, again consistent with prior round JICF observations (Getsinger *et al.* 2014). The presence of a tab, either at the upstream or downstream location, tended to make the vorticity field more symmetric, though the results were not exactly the same for these two different tabbed configurations.

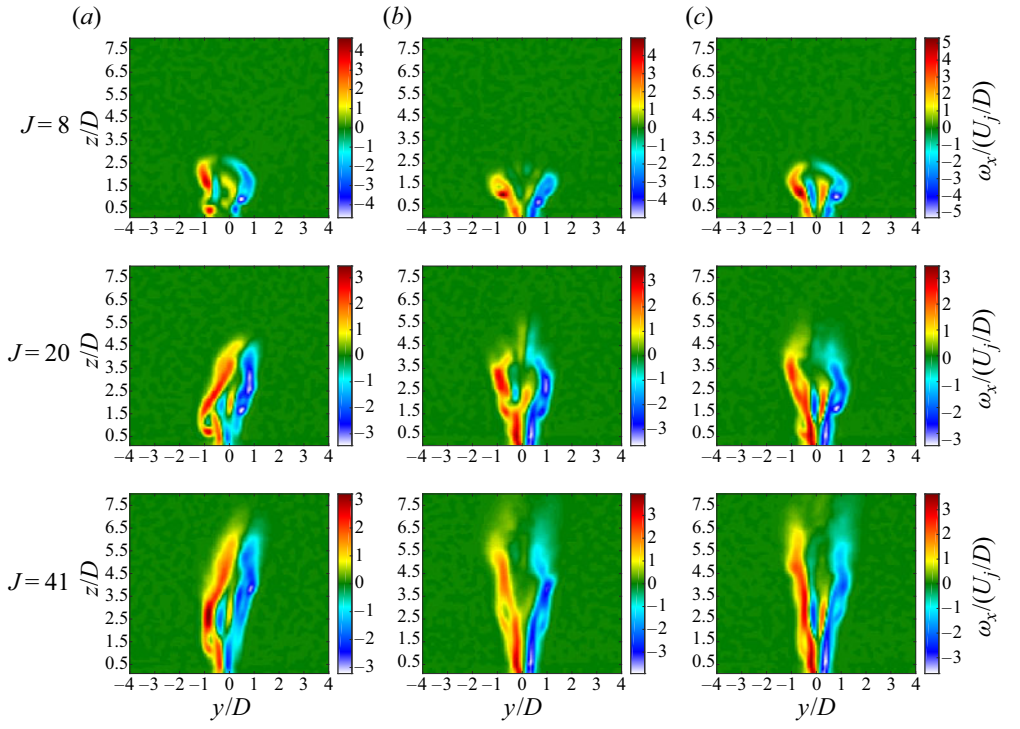

Figure 14. Mean cross-sectional vorticity images at the cross-sectional location $x/D = +0.5$. Images correspond to the (*a*) non-tabbed jet, (*b*) tab upstream jet and (*c*) tab downstream jet, for the AU jet near the critical transition at $J = 8$ and CU jets at $J = 20$ and $J = 41$, all with $Re_j = 1900$. The colourbars are scaled to the maximum and minimum vorticity values contained within each image shown.

This near-field cross-sectional symmetry was also seen at lower J values further downstream in high-resolution PLIF results (figure 7*b*,*c*). At higher J (figure 8*b*,*c*), in contrast, the far-field cross-sections were altered by upstream and downstream tabs, yet were still strongly asymmetric.

Symmetry breaking tab orientations were also explored in simultaneous PLIF/PIV experiments to determine the implications of positioning an asymmetrically oriented tab at the exit plane and thus creating an azimuthal vorticity distribution for the development of the CVP, recalling that Peterson & Plesniak (2004) suggested such an asymmetric distribution could give rise to asymmetries in the jet further downstream. Recall from figures 7 and 8 that the high-resolution PLIF imaging of a tabbed jet showed that as the tab orientation was azimuthally rotated away from the upstream edge of the jet, the cross-sectional structure showed a bulk deflection of the jet away from the location (right vs left) of the tab, and as the momentum flux ratio increased, the tab was able to produce more pronounced alterations to the naturally asymmetric jet cross-sectional structure. For comparison, figure 15 shows instantaneous centreplane vorticity images and mean cross-sectional vorticity images at $x/D = +0.5$ for symmetry breaking tab orientations at $J = 5$, the flow condition for which tabs had a more dramatic effect on USL instabilities. The centreplane vorticity field showed a rather significant delay in the initiation and strengthening of the USL instabilities and vortex rollup for a tab placed closer to the upstream region (e.g. L15). As the tab was moved azimuthally about the jet periphery, the delay in USL vortex rollup was lessened, to the point where, by position L30

or L45, and definitely by L90 (or R90), there was very little discernible difference with respect to the jet with the non-tabbed simple extension in figure 15. In terms of the mean cross-sectional vorticity in the figure, the azimuthally placed tabs at L15 and L30 tended to introduce asymmetry at the jet exit, generally consistent with asymmetric cross-sectional high-resolution PLIF images of the JICF under similar conditions in figure 7.

For the JICF at a higher momentum flux ratio, the naturally asymmetric cross-section was more significantly influenced by specific tab locations. Instantaneous centreplane and mean cross-sectional vorticity fields at $J = 41$ are shown in figure 16. Close inspection indicates that the left and right oriented tabs at the 'extreme' conditions L90 and R90 actually produced different delays in the USL vorticity rollup, and the cross-sectional vorticity fields were also different from one another (and were asymmetric with respect to the jet centreplane). These differences were manifested further downstream in high-resolution PLIF experiments in figure 8, with a perceptible deflection of the jet and vorticity field away from the location of the tab. The slight difference in the asymmetric vorticity production between the tab 90° to the left or right of the upstream may be a result of the inherent asymmetry already present in the transverse jet at $J = 41$.

3.5. *POD analysis and counter current shear layer analogy*

The tab's influence on other dynamics within the transverse jet flow field may be explored via snapshot POD (Sirovich 1987) applied to the velocity vector fields from the centreplane stereo-PIV imaging. This approach has been explored in additional studies of the JICF (Meyer, Pedersen & Özcan 2007; Schlatter *et al.* 2011; Gevorkyan *et al.* 2018) as a means of extracting mode structures from instantaneous snapshots of the flow and identifying dominant instabilities in the flow field. In the present studies, snapshot POD analysis was applied to all 500 instantaneous realizations of the flow field for each test case considered, well above the 300 snapshots required for statistical convergence (Shoji 2017). The resolved mode structures were ordered in terms of their respective magnitudes of total kinetic energy fluctuation, helping to reveal characteristic flow features and dynamics which might otherwise be hidden or masked by the chaotic flow field. Figures 17, 18 and 19 depict the four most energetic mode structures, along with their respective contributions to the total kinetic energy fluctuation, for the transverse jet without a tab, with the tab upstream and with the tab downstream at momentum flux ratios of $J = 5$, $J = 8$ and $J = 41$, respectively. Only $J = 41$ had an USL which was clearly CU in the absence of a tab (Shoji *et al.* 2020*b*). The non-tabbed mode structures over the momentum flux ratio range in question (figures 17*a*–19*a*) agreed quite well with the dynamics seen in the snapshot POD for the flush nozzle-injected JICF for the same range by Gevorkyan *et al.* (2018), even when the latter did not include a thin circular extension as in the present experiments. In the non-tabbed jet mode plots, for all three J values, the first two most dominant modes displayed isolated structures within the shear layer of the jet, and as the momentum flux ratio decreased, these modes were initiated closer to the jet exit, much like the vortex rollup and shear layer instability characteristics. As noted in Gevorkyan *et al.* (2018), such isolation of the mode structures in the shear layer agrees with dynamic mode decomposition analysis of DNS JICF studies by Iyer & Mahesh (2016). For low momentum flux ratios, especially at $J = 5$ but also at $J = 8$, the structures were contained entirely within the USL of the jet, while at higher momentum flux ratios, as shown by modes one and two at $J = 41$ (figure 19*a*(1)–*a*(2)), the dominant mode structures spanned the upstream and downstream shear layers, and appeared to be merged. This was analogous to the expansion of the wavemaker region to the downstream shear layer as documented in the DNS by Regan & Mahesh (2019), and the origination of the dominant eignenmode

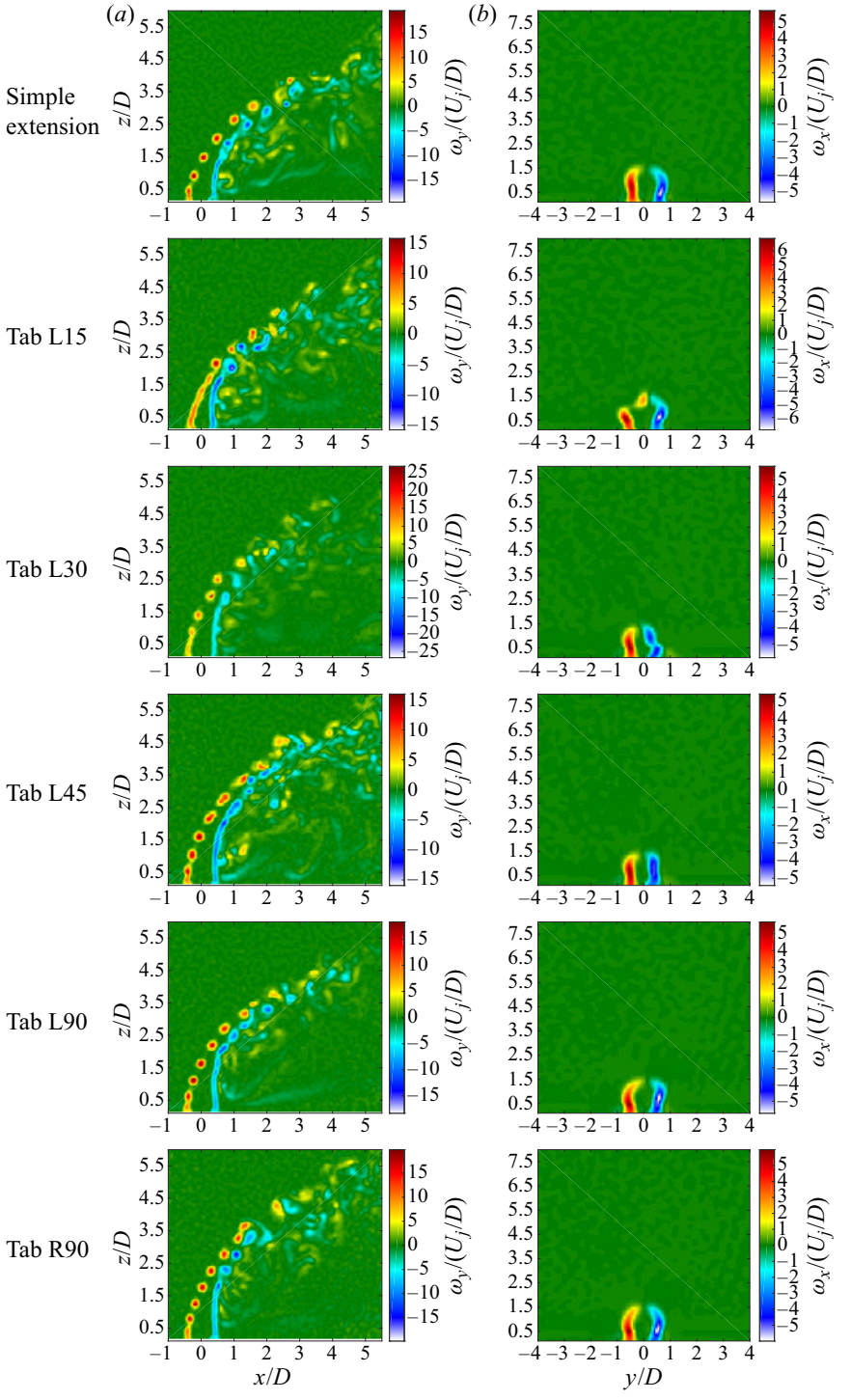

Figure 15. Images of (*a*) the instantaneous centreplane and (*b*) mean cross-sectional vorticity fields for $J = 5$ and $Re_j = 1900$ at $x/D = 0.0$. Symmetry breaking tab orientations are shown. The colourbars are scaled to the maximum and minimum vorticity values contained within each image shown.

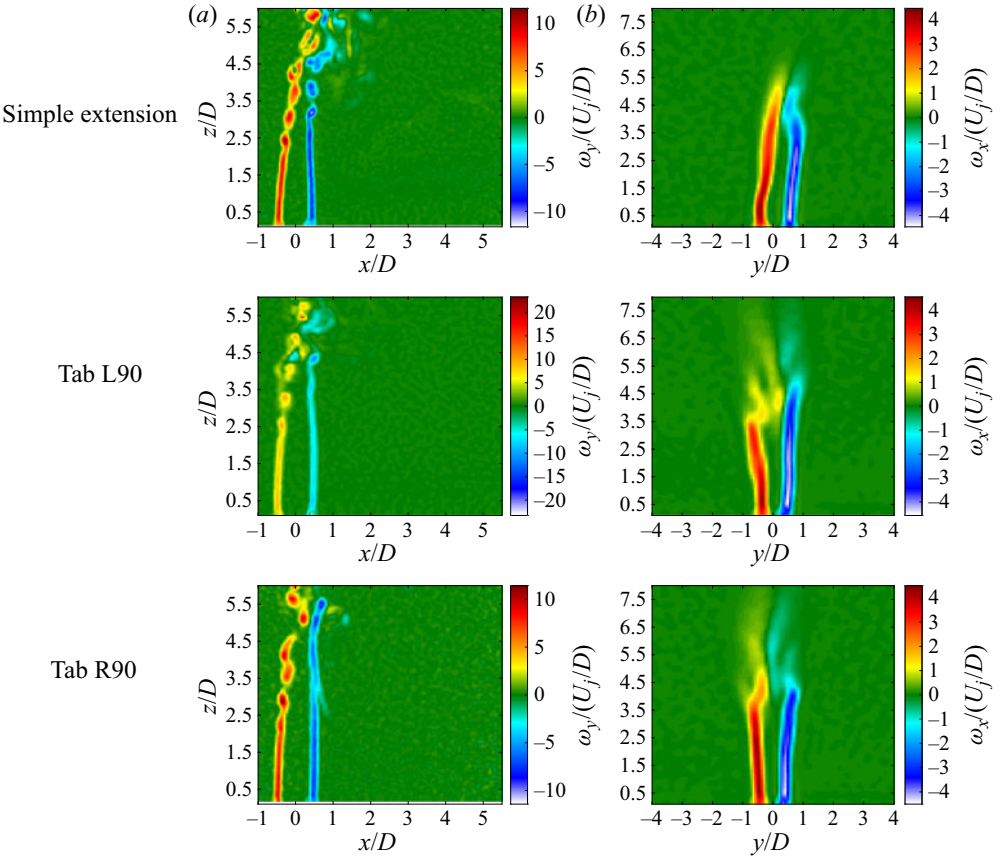

Figure 16. Images of (*a*) the instantaneous centreplane and (*b*) mean cross-sectional vorticity fields for $J = 41$ and $Re_j = 1900$ at $x/D = 0.0$. Selected symmetry breaking tab orientations are shown. The colourbars are scaled to the maximum and minimum vorticity values contained within each image shown.

on the downstream side of the jet as shown in Regan & Mahesh (2017), both for a CU jet at $J = 16$ and $Re_j = 2000$. It is also noted that the wake structures were more pronounced in figures 17(*a*)–19(*a*) as the momentum flux ratio was decreased and as the jet became more bent over. The increasing contribution of the wake structures resulted in a decreasing energy content contained within the jet shear layer modes, reducing the energy content within the first mode from 11 % to 7 % in changing from $J = 41$ to $J = 5$. These wake features were most dominant in the non-tabbed jet at $J = 5$ (figure 17*a*(3)–*a*(4)), where large scale structures denoting in- and out-of-plane velocity form in the jet wake. Gevorkyan *et al.* (2018) and Fric & Roshko (1994) note such structures are largely associated with the wake vortices which act to entrain crossflow boundary layer fluid up into the jet.

Placement of the tab in the upstream region of the jet exit, as seen in the vorticity field in § 3.4, and in the USL stability (§ 3.1), structure (§ 3.2) and mixing results (§ 2.1) from the high-resolution PLIF experiments, created the most significant alterations to the JICF flow field. The POD modes for each of the corresponding momentum flux ratios ($J = 5$, 8 and 41 in figures 17*b*, 18*b* and 19*b*, respectively) reaffirmed these observations. It was observed that the energy content contained within the first two (nominally shear layer)

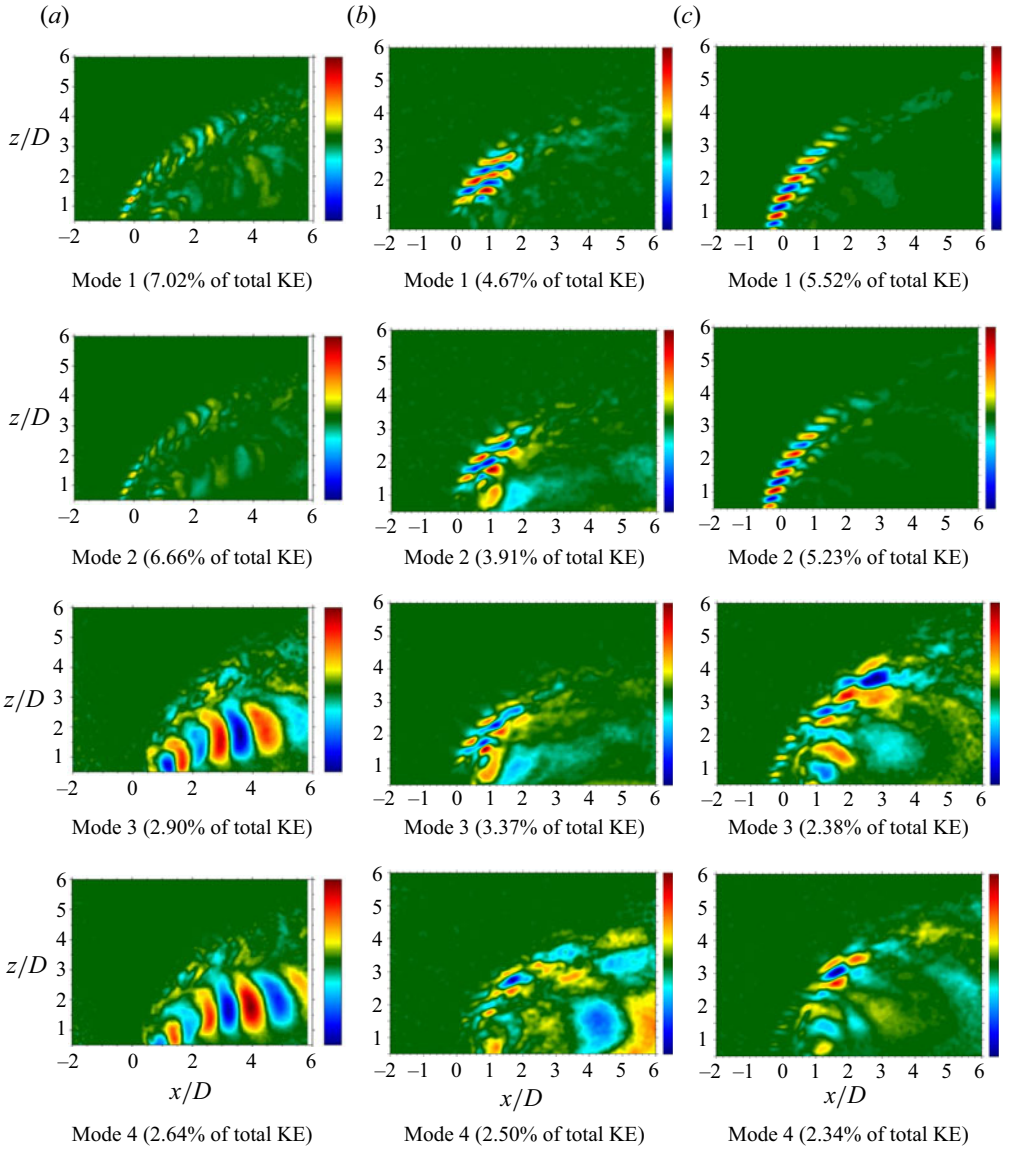

Figure 17. Particle image velocimetry based POD mode structures extracted from the centreplane velocity field at $J = 5$ and $Re_j = 1900$, for (*a*) the non-tabbed jet, (*b*) the tab upstream and (*c*) the tab downstream. The respective percentages of total kinetic energy fluctuation content are shown. The colourbar in each image represents the mode scaled by its own norm and the mean jet velocity at the jet exit U_j.

modes was decreased as compared with the non-tabbed JICF at the same flow conditions, hence, with a weakening of the USL vorticity dynamics. As momentum flux ratio was decreased, the differences in energy content between the non-tabbed and upstream tabbed jets became smaller in magnitude, though the mode structures became much more different from one another, e.g. for the first two modes at $J = 5$ in figure 17. These observations were likely related to the increasing significance of the wake structures as the jet became more bent over, with a transfer of kinetic energy from the USL to the wake structures; this trend was not necessarily associated with the presence of the tab. The overall differences

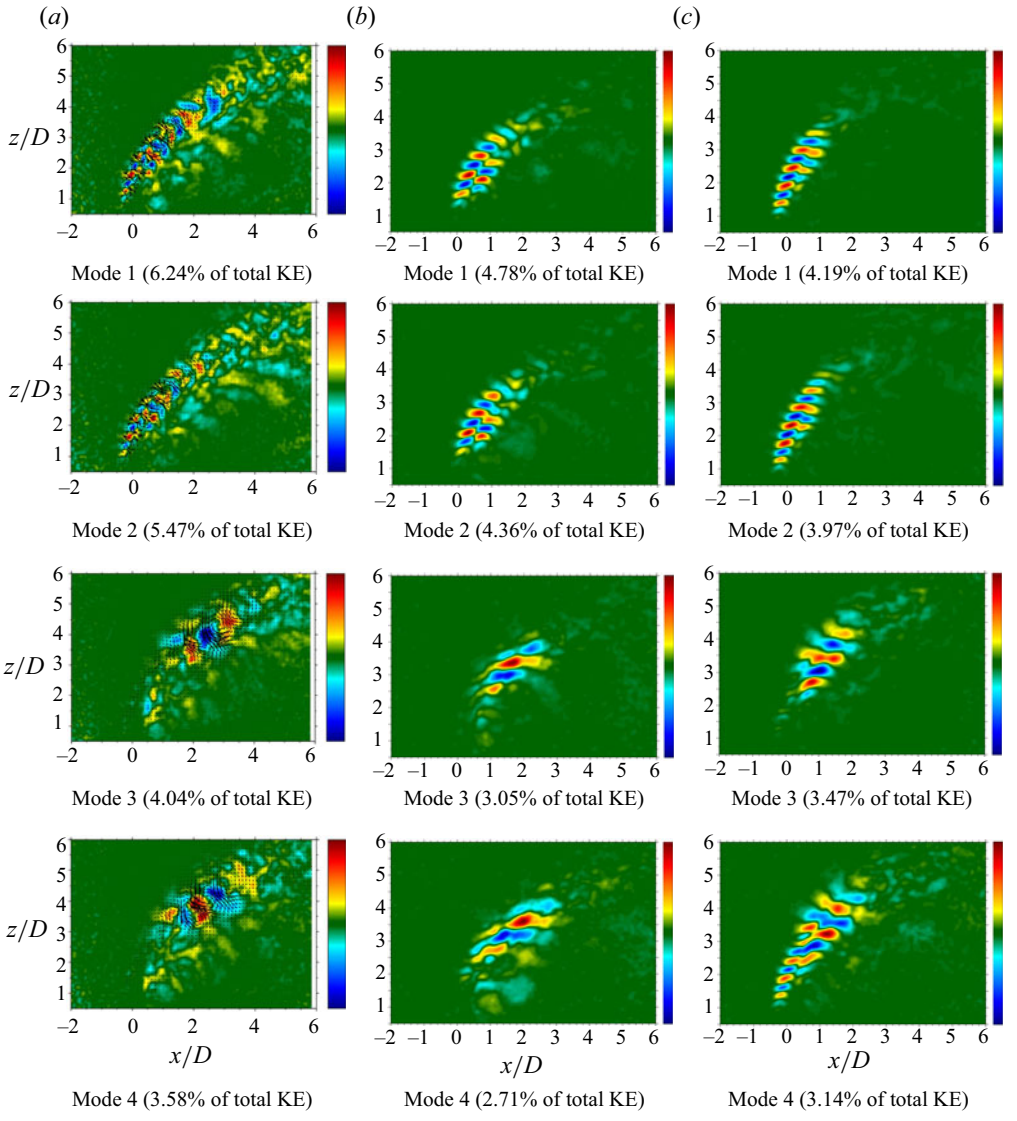

Figure 18. Particle image velocimetry based POD mode structures extracted from the centreplane velocity field at $J = 8$ and $Re_j = 1900$, for (*a*) the non-tabbed jet, (*b*) the tab upstream and (*c*) the tab downstream. The respective percentages of total kinetic energy fluctuation content are shown. The colourbar in each image represents the mode scaled by its own norm and the mean jet velocity at the jet exit U_j.

in the most energetic mode shapes for $J = 5$, however, with a broadened region over which oscillations occurred with the upstream tab, were clearly the result of the tab placement. Similar mode shape alterations as well as a transfer of energy from shear layer to wake structures was observed for the upstream tab with $J = 8$ in the figures in 18(*b*), though to a lesser degree than for $J = 5$. Given that $J = 41$ produced a JICF that was largely upright, the presence of wake structures was not detected, and, thus, even in the presence of the tab upstream, did not demonstrate a dramatic decrease in the energy content of the modes. When the tab was placed in the downstream edge of the jet, alterations in the mode structure and energy transfer from the shear layer to the wake were similar to

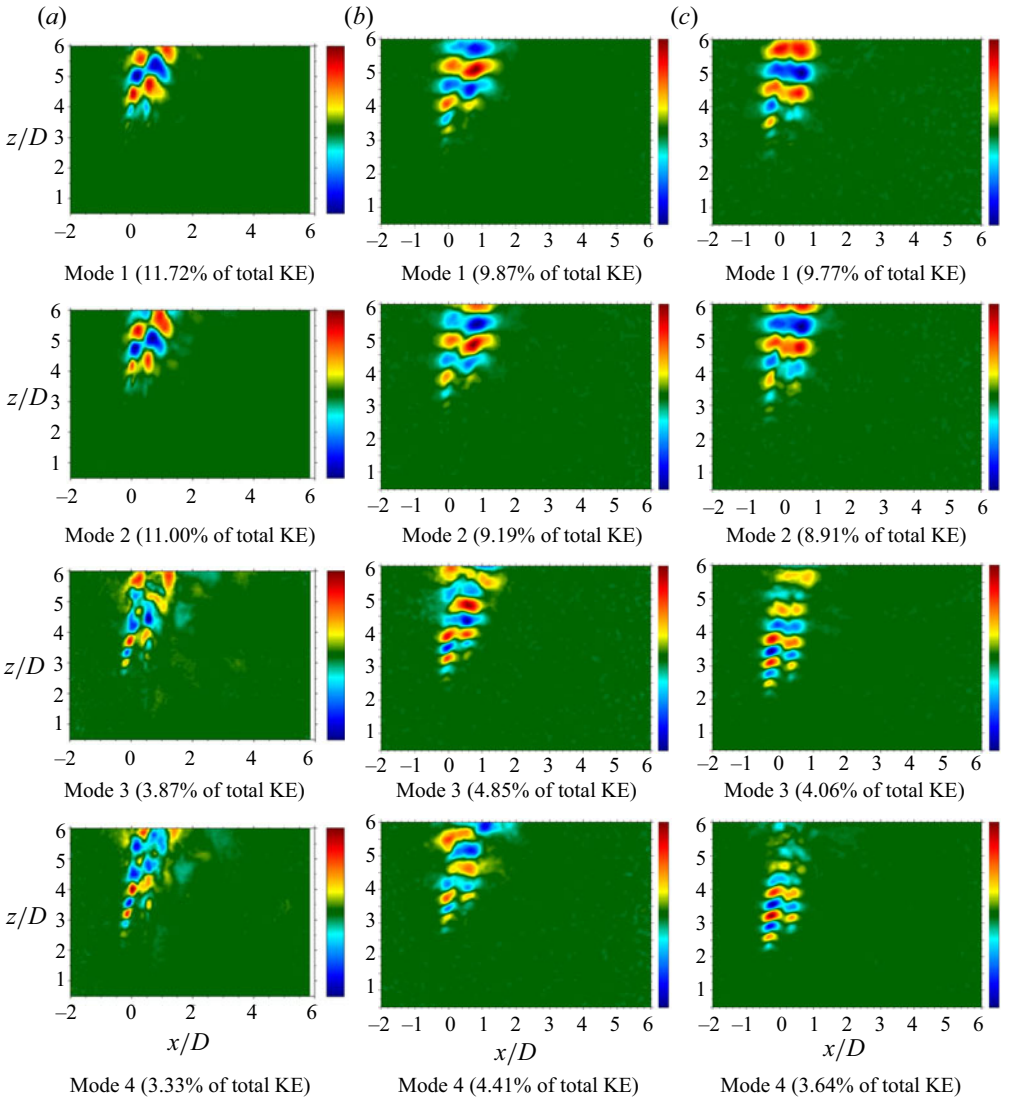

Figure 19. Particle image velocimetry based POD mode structures extracted from the centreplane velocity field at $J = 41$ and $Re_j = 1900$, for (*a*) the non-tabbed jet, (*b*) the tab upstream and (*c*) the tab downstream. The respective percentages of total kinetic energy fluctuation content are shown. The colourbar in each image represents the mode scaled by its own norm and the mean jet velocity at the jet exit U_j.

effects observed for the upstream tabs at $J = 8$ and especially at $J = 41$, but there were greater differences between downstream and upstream tab results for $J = 5$. There were clear upstream and downstream mode structures in the first and second POD modes for the downstream tab with $J = 5$ (figure 17*c*) as compared with the non-tabbed insert in figure 17(*a*), which only displayed clear USL structures. This observation was consistent with hotwire-based alterations in spectral characteristics of the naturally AU JICF when the tab was placed downstream; the downstream tab as well as the upstream tab weakened the USL's instabilities.

Proper orthogonal decomposition analysis also enables one to analyse the fluctuations in magnitude of the respective mode coefficients across the series of original snapshots,

as has been done by Meyer *et al.* (2007) and Gevorkyan *et al.* (2018), and, thus, to study correlations in the evolution of the dynamics in the flow. When treating a specific snapshot image, the magnitude of each respective coefficient represents the contribution of that particular mode in forming a summation from all of the modes to reconstruct the snapshot. If the mode coefficients from select mode pairs are then plotted against one another, it is possible to determine if the respective modes are at all correlated in their evolution over time. Gevorkyan *et al.* (2018) demonstrated for the AU jet at $J = 5$ that when the first two mode coefficients are plotted against one another for all 500 snapshots, the plot resembles that of a ring, representative of a periodic travelling wave, and that the dominant jet dynamical behaviour may be characterized by linear combinations of the first two modes. For the JICF at larger J values with a CU USL, however, Gevorkyan *et al.* (2018) showed that the ring-like plot of the first two mode coefficients deteriorates to a diffuse blob, where no periodic travelling wave behaviour is detectable. Instead the coefficient plots rightly illustrate the broadband frequency content of shear layer instabilities in a CU flow, consistent with corresponding hotwire measurements of the USL. An understanding of the effects of tabs on JICF dynamical characteristics can benefit from this approach as well.

Figure 20 shows plots comparing the coefficients of the first two most energetic proper orthogonal modes for the flow field at $J = 5$ for the non-tabbed jet with a simple thin extension, and for tab placements in the upstream, downstream and symmetry breaking tab orientations about the jet exit periphery. Clearly, as was seen by Gevorkyan *et al.* (2018) for the flush nozzle-injected jet at $J = 5$, the coefficient plot for the non-tabbed jet created a ring, indicative of a travelling wave phenomena associated with the USL structures, as expected for an AU flow. When the tab was then placed in the upstream position, the ring like representation was not recovered, and instead a diffuse blob was formed, typical of a CU flow. This finding was not unexpected in that spectral contour plots from the high-resolution PLIF experiments documented a transition in the USL instabilities from absolute to convective instability with the tab upstream for $J = 7$ and $Re_j = 2300$. There was also a slight transition in the shear layer instabilities when the tab was positioned downstream, although the coefficient plots retained the ring shape overall, suggesting here that the flow remained AU at $J = 5$ for such a tab placement. The high-resolution PLIF instability characteristics in figure 5(*d*) were actually for a momentum flux ratio closer to the critical transition between absolute and convective instability ($J = 7$), and, hence, was more likely to be affected by small alterations in the flow such as a downstream tab. In contrast, the momentum flux ratio of $J = 5$ in the simultaneous imaging experiments was more strongly AU and, thus, further from the critical transition for these flow conditions. Hence, for the strong AU flow at $J = 5$, the weaker influence of the tab downstream resulted in the flow's remaining AU in POD mode coefficient plots. This observation was also seen in the USL vorticity generation for the downstream tab at $J = 5$ in figure 11; its instantaneous structure was remarkably similar to that of the non-tabbed jet, but was quite different from that of the tab positioned at the upstream. The coefficient plots in figure 21 for $J = 8$ reinforced this idea of the impact of the tab being dependent on the closeness of the USL instability state to absolute instability conditions. The non-tabbed jet here was still AU, though more weakly so as it was closer to the critical transition around $J \approx 9$–10, and when the tab was placed in either the upstream or downstream, the resulting coefficient plot showed more diffuse blobs rather than a circle, as would be expected for a flow field that was CU. Further extension of this evaluation to tab configurations at $J = 41$ in figure 22 showed the expected diffuse blobs in the coefficient plots for all tab orientations, as the flow is known to be naturally CU, and the tab acted to further weaken the flow field instabilities.

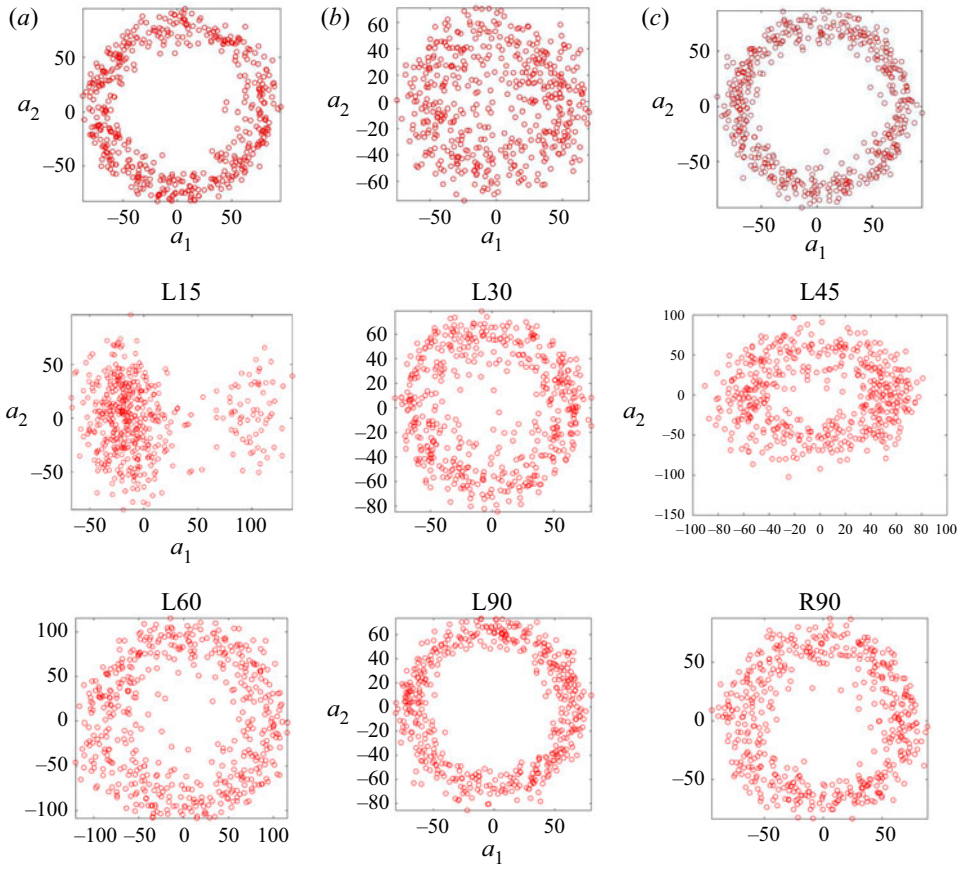

Figure 20. Particle image velocimetry based POD coefficients of the first two modes plotted against each other. Data are extracted from the centreplane velocity field at $J = 5$ and $Re_j = 1900$, for a variety of tab configurations. (*a*) Simple extension. (*b*) Tab upstream. (*c*) Tab downstream. Other tab locations are as labelled.

Interestingly, the resulting coefficient plots for symmetry breaking tab orientations for all three momentum flux ratios were generally consistent with the trends in USL spectra from the high-resolution PLIF experiments in § 3.1, as well as the vorticity analysis in § 3.4, demonstrating that the influence of the tab was most significant when the USL was naturally strongly AU. For the flow at $J = 5$, in figure 20, besides the upstream tab, there were additional alterations in the coefficient plots, though not as severe, when the tab was situated at L15 and L45 positions. Separate studies (Harris 2020) show downstream cross-sectional asymmetries for such cases, with a more significant bulk deflection of the CVP. The altered (non-blob-like) structures for these two cases in figure 20 suggested additional complexity in the dynamics that could warrant further exploration. As for the other cases, for $J = 8$ in figure 21, only the downstream, L30, and possibly L60 tab configurations showed some evidence of periodicity in the flow, while other cases indicated weakening of the disturbances to become like a CU flow field. For $J = 41$ in figure 22, the coefficient plots showed no significant alterations with the presence of tabs at any position, generally consistent with spectral characteristics and centreplane imaging for the CU JICF from the high-resolution PLIF experiments.

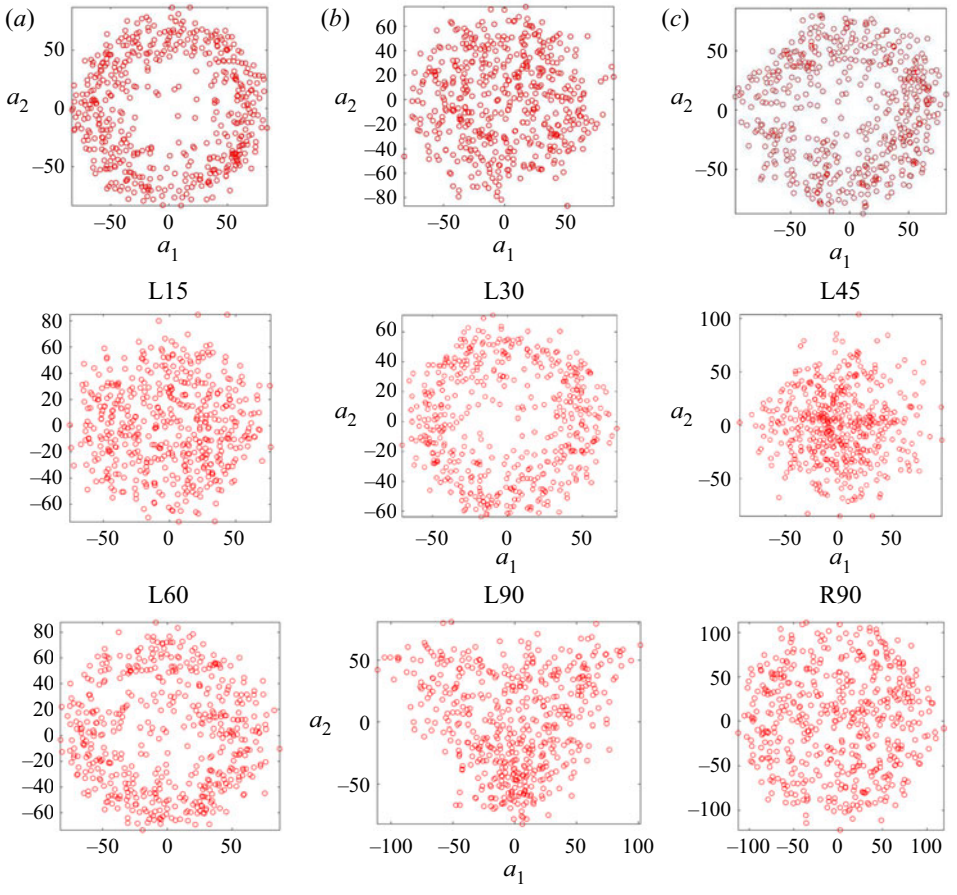

Figure 21. Particle image velocimetry based POD coefficients of the first two modes plotted against each other. Data are extracted from the centreplane velocity field at $J = 8$ and $Re_j = 1900$, for a variety of tab configurations. (*a*) Simple extension. (*b*) Tab upstream. (*c*) Tab downstream. Other tab locations are as labelled.

In addition to the vorticity field and POD analysis of the velocity field extracted from the present experiments, the local velocity field in the vicinity of the upstream region of the jet exit for different tab (and tabless) configurations was also examined. The origins of the transition in the transverse jet's USL instabilities can be understood in the context of viewing the USL near the flush jet exit as a counter-current shear layer (CCSL) where the effect of blockage of the crossflow by the jet column creates a local negative velocity upstream of the USL adjacent to a local positive vertical velocity within the jet, per the ideas of Iyer & Mahesh (2016). When the CCSL velocity ratio is large enough, the counterflow between the streams can create transition from convective to absolute instability in the shear layer, as one would observe for the planar CCSL (Huerre & Monkewitz 1985; Strykowski & Niccum 1991). Extensive experimental studies of this near-field region of the JICF for a range of J values in Shoji *et al.* (2020*b*) demonstrated a general consistency in the CCSL model in understanding transverse jet USL transition to absolute instability. Shoji *et al.* (2020*b*) also demonstrated that as the upstream momentum thickness of the exiting jet becomes larger, the degree or strength of counter-current flow required to cause transition from CU to AU increases. Hence, for the same crossflow and jet bulk velocity conditions, a thicker upstream momentum thickness θ could create a

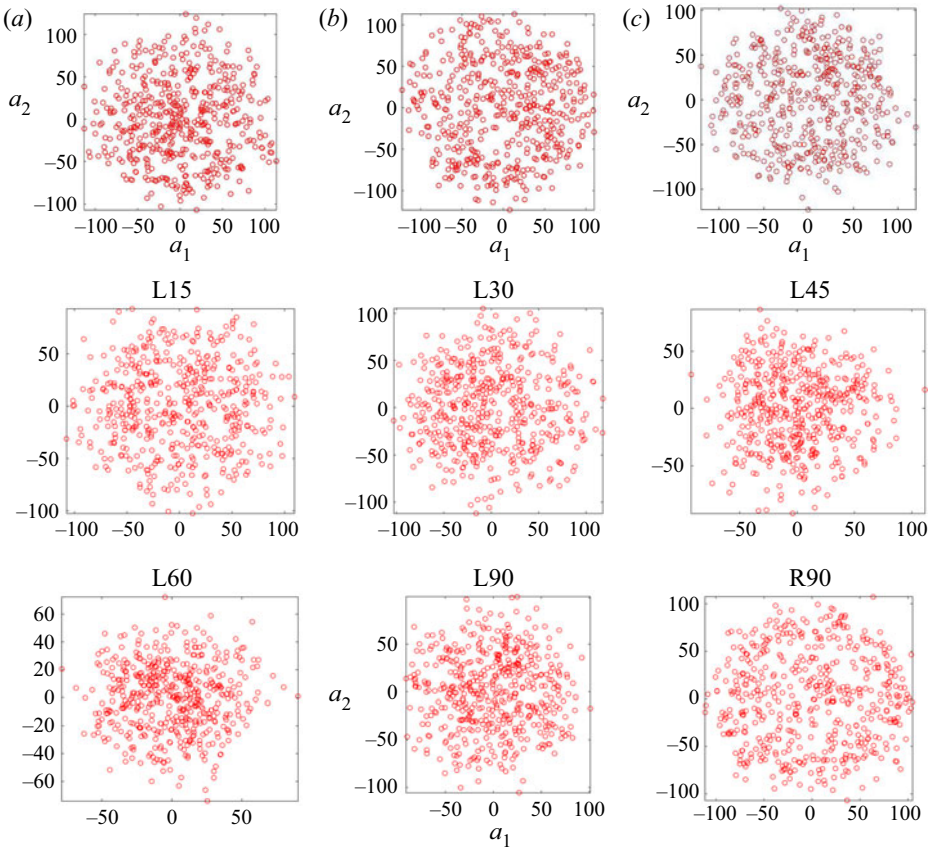

Figure 22. Particle image velocimetry based POD coefficients of the first two modes plotted against each other. Data are extracted from the centreplane velocity field at $J = 41$ and $Re_j = 1900$, for a variety of tab configurations. (*a*) Simple extension. (*b*) Tab upstream. (*c*) Tab downstream. Other tab locations are as labelled.

weaker instability in the USL; this is also consistent with a diminished growth rate of the axisymmetric instability mode for the high momentum flux ratio JICF (Alves *et al.* 2008). Such measurements of the velocity in these experiments enabled exploration of the influence of the tabs on the local USL flow field in the context changes in the jet's upstream momentum thickness.

To explore the effect of a tab placed at various locations on the upstream jet momentum thickness θ, the velocity field in the x–z plane at the upstream region of the jet near the jet exit, extracted from PIV measurements, was used, with details on the method of extraction described in Shoji *et al.* (2020*b*). This method was applied to all jet configurations here, including a range of tab positions. The results for $J = 5$ for various tab orientations are given in table 1, where the scaled upstream momentum thickness θ/D, and state of the USL as determined via hotwire anemometry (AU or CU) are given. The data in table 1, and the corresponding data for $J = 8$ in table 2, showed a correspondence between the larger values of θ and the observed state of the USL per hotwire measurements, which, interestingly, were also consistent with the POD coefficient plots. Even when the tab was placed azimuthally at a position well away from the jet's USL, the small and moderate increases in upstream momentum thickness θ were consistent with the altered state of the jet's dynamics as observed in the hotwire measurements and in POD coefficient plots.

Template configuration	θ/D	Experiment USL
Simple extension	0.0304	AU
Tab upstream	0.0405	CU
Tab L90	0.0322	AU
Tab R90	0.0315	AU
Tab downstream	0.0363	AU

Table 1. For $J = 5$ and $Re_j = 1900$, the upstream jet momentum thickness at the jet exit (scaled by D) and the hotwire-based state of the USL.

Template configuration	θ/D	Experiment USL
Simple extension	0.0293	AU
Tab upstream	0.0376	CU
Tab L90	0.0323	CU
Tab R90	0.0314	CU
Tab downstream	0.0349	CU

Table 2. For $J = 8$ and $Re_j = 1900$, the upstream jet momentum thickness at the jet exit (scaled by D) and the hotwire-based state of the USL.

We also note that the momentum thickness of the jet was significantly increased over the non-tabbed jet when the tab was upstream, and moderately so when the tab was downstream. Thickening of the momentum thickness was typically reduced as the tab orientation was rotated away from the upstream, having the least impact when placed directly in the sides of the jet. As stated for the POD coefficient plots, some unusual behaviour in the shear layer dynamics may be due to the large asymmetric deflection of the jet structure, whereby the shear layer dynamics were not entirely captured in the centreplane view of the evolving jet. Also possible is that asymmetric instabilities may be initiated and growing to compete with the axisymmetric mode, such that analysis of the periodicity of the USL from the coefficient plots may not be accurately recovered due to coupling of the instability modes, which would contaminate the simple periodic behaviour.

4. Discussion and conclusions

The present experimental study documented the effects of simple passive control of a JICF via a small triangular tab placed about the periphery of the jet exit. Effects on jet shear layer instabilities, structure, mixing and dynamical features were quantified. The study extended the flow regimes and geometrical parameter space examined in previous works on tabbed jets in crossflow, taking advantage of contemporary diagnostics and more recent observations of a transition in the USL in the absence of tabs (Megerian *et al.* 2007), and then exploring tabs at conditions for which the USL in the absence of the tab was CU and AU. The presence of a tab was seen to weaken and delay the initiation of the USL instability in both flow regimes, in some cases rather extensively, where the significance of such alterations were generally dependent upon the original strength of the instability in the absence of a tab, and the relative location of the tab with respect to the upstream edge of the jet exit.

From the high-resolution PLIF imaging, it was seen that in many ways the effect of the single tab on the naturally AU JICF with $J = 7$ was different, from a stability and structural perspective, from the tab's effect on the naturally CU jet with $J = 61$. The tab caused the $J = 7$ AU USL to become effectively CU for most orientations, especially when positioned closer to the upstream region (figure 5), and yet the effect on the jet cross-sectional structure was relatively small, with a flattening or introduction of slight asymmetries in the CVP (figure 7). The slight asymmetries were consistent with such weakening in the USL instabilities, though the dramatic changes in spectral characteristics might imply greater changes than those actually observed in the jet structure. In contrast, the tab caused the USL for the $J = 61$ JICF to weaken when placed at the upstream location, but beyond that point there was little discernible change to the spectral characteristics (figure 6). Yet the effects of the tab position on the jet's cross-sectional structure, even when there was little obvious change in the USL, were quite significant (figure 8), leading to apparent flipping of the asymmetric CVP-like structure, though the specific downstream location at which the image slice was taken could influence this orientation. While there was a logical connection between tab-generated shear layer characteristics and jet structural alteration, a more consistent connection was observed between the predicted wavemaker regions for AU and CU jets from the work of Regan & Mahesh (2019) and the tab orientations having the greatest effects. For naturally AU shear layers such as with $J = 7$, the wavemaker region in the upstream region was consistent with the effectiveness of tab placement in that region (e.g. figure 7*b*), while for $J = 61$, the wavemaker's extending along the entire USL of the jet and wrapping around the jet suggested the effectiveness of perturbation or jet placement at multiple locations around the jet periphery. While there are limited computational conditions to enable direct comparisons, the correspondence here is intriguing, and bears more extensive exploration. Despite these differences in specific tab influence on the JICF in these two different regimes, the overall effects of the tab on jet molecular mixing were similar in terms of the degree of reduction in unmixedness (figures 9 and 10), though there were some specific differences, even between left and right orientations of the tab, clearly relating to the natural asymmetries in jet cross-sectional structure.

The simultaneous stereo PIV and acetone PLIF experiments enabled more extensive examination of the vorticity dynamics associated with a gaseous JICF and its alteration by the tab situated at various locations within the jet periphery. In terms of centreplane-based vorticity evolution, placement of a tab in the upstream or near-upstream location caused a delay in USL rollup and a reduction in USL vorticity associated with a thickening of the upstream jet momentum thickness. This delay was seen irrespective of the J range, that is, whether the USL was naturally AU or CU in the absence of a tab (figures 11, 13 and 15). The influence of downstream tab placement or tab placement much further from the upstream, e.g. at or beyond 45° from the upstream location, was observed to have a rather minimal effect on the USL instability delay, though in most cases such placement had a significant symmetrizing influence on near-field cross-sectional vorticity dynamics. This influence on cross-sectional vorticity generation and evolution very close to the jet exit could be used to explain rather significant alterations in far-field cross-sectional shape and symmetry observed in corresponding PLIF-only experiments, which in turn did contribute to an improvement in molecular mixing. But specific positioning of the tab for a given set of flow conditions, especially at higher J values where there was a naturally asymmetric cross-sectional orientation, could have different effects on the vorticity. Hence, the current studies and methods could contribute to a database for determining optimal jet/tab configurations for given flow conditions.

Proper orthogonal decomposition modes extracted from centreplane velocity field measurements showed significant influence of tab placement on jet upstream and downstream vorticity as well as wake structures, again, depending on J. Phase portraits extracted from POD mode coefficient plots produced periodic (circular) shapes for tab placement corresponding to conditions for which the USL was determined in hotwire measurements and instantaneous vorticity fields to be AU. This suggests that dynamical characteristics revealed through POD mode shapes and coefficient plots could be used to develop characteristic signatures for transverse jet behaviour that relate directly to their structure and scalar mixing characteristics.

The present study involved a rather wide parameter space to generate such signatures for various J values, tab positions and visualization orientations. However, there are additional parameters which could be varied to study the flow for optimization purposes. Contemporary modelling tools, e.g. methods for evolving reduced-order models for the flow field, could be very useful for predicting the most effective configurations for given applications and flow conditions, and this is a subject of ongoing investigation.

Funding. This research has been supported by the National Science Foundation under grants CBET-1437014 and CBET-1933310 and by the Air Force Office of Scientific Research under grants FA9550-15-1-0261 and FA9550-19-1-0191.

Declaration of interests. The authors report no conflict of interest.

Author ORCIDs.
A.R. Karagozian https://orcid.org/0000-0002-2847-8773.

References

Ahuja, K.K. & Brown, W.H. 1989 Shear flow control by mechanical tabs. *AIAA Paper* 89-0994.

Alves, L.S.D.B., Kelly, R.E. & Karagozian, A.R. 2007 Local stability analysis of an inviscid transverse jet. *J. Fluid Mech.* **581**, 401–418.

Alves, L.S.D.B., Kelly, R.E. & Karagozian, A.R. 2008 Transverse-jet shear-leyer instabilities. Part 2. Linear analysis for larger jet-to-crossflow velocity ratio. *J. Fluid Mech.* **602**, 383–401.

Bagheri, S., Schlatter, P., Schmid, P.J. & Henningson, D.S. 2009 Global stability of a jet in crossflow. *J. Fluid Mech.* **624**, 33–44.

Bohl, D.G. & Foss, J.F. 1995 Characteristics of the velocity and streamwise vorticity fields in a developing tabbed jet. *AIAA Paper* 95-0102.

Bradbury, L.J.S. & Khadem, A.H. 1975 The distortion of a jet by tabs. *J. Fluid Mech.* **70** (4), 801–813.

Bunyajitradulya, A. & Sathapornnanon, S. 2005 Sensitivity to tab disturbance of the mean flow structure of nonswirling jet and swirling jet in crossflow. *Phys. Fluids* **17** (4), 045102.

Carletti, M.J., Rogers, C.B. & Parekh, D.E. 1996 Parametric study of jet mixing enhancement by vortex generators, tabs, and deflector plates. *ASME Publ. FED* **237**, 303–312.

Cortelezzi, L. & Karagozian, A.R. 2001 On the formation of the counter-rotating vortex pair in transverse jets. *J. Fluid Mech.* **446**, 347–373.

Davitian, J., Getsinger, D., Hendrickson, C. & Karagozian, A.R. 2010*a* Transition to global instability in transverse-jet shear layers. *J. Fluid Mech.* **661**, 294–315.

Davitian, J., Hendrickson, C., Getsinger, D., M'Closkey, R.T. & Karagozian, A.R. 2010*b* Strategic control of transverse jet shear layer instabilities. *AIAA J.* **48** (9), 2145–2156.

Fearn, R. & Weston, R. 1974 Vorticity associated with a jet in a crossflow. *AIAA J.* **12**, 1666–1671.

Fric, T.F. & Roshko, A. 1994 Vortical structure in the wake of a transverse jet. *J. Fluid Mech.* **279**, 1–47.

Getsinger, D.R., Gevorkyan, L., Smith, O.I. & Karagozian, A.R. 2014 Structural and stability characteristics of jets in crossflow. *J. Fluid Mech.* **760**, 342–367.

Getsinger, D.R., Hendrickson, C. & Karagozian, A.R. 2012 Shear layer instabilities in low-density transverse jets. *Exp. Fluids* **53**, 783–801.

Gevorkyan, L. 2015 Structure and mixing characterization of variable density transverse jet flows. PhD dissertation, University of California, Los Angeles.

Gevorkyan, L., Shoji, T., Getsinger, D.R., Smith, O.I. & Karagozian, A.R. 2016 Transverse jet mixing characteristics. *J. Fluid Mech.* **790**, 237–274.

GEVORKYAN, L., SHOJI, T., PENG, W.Y. & KARAGOZIAN, A.R. 2018 Influence of the velocity field on scalar transport in gaseous transverse jets. *J. Fluid Mech.* **834**, 173–219.

GUTMARK, E. & HO, C.M. 1983 On the preferred modes of the spreading rates of jets. *Phys. Fluids* **26**, 2932–2938.

HARRIS, E.W. 2020 As of yet: Untitled. PhD thesis, University of California, Los Angeles.

HAVEN, B.A. & KUROSAKA, M. 1997 Kidney and anti-kidney vortices in crossflow jets. *J. Fluid Mech.* **352**, 27–64.

HENDRICKSON, C. 2012 Identification and control of the jet in crossflow. PhD thesis, University of California, Los Angeles.

HUERRE, P. & MONKEWITZ, P.A. 1985 Absolute and convective instabilities in free shear flows. *J. Fluid Mech.* **159**, 151–168.

HUSSAIN, A.K.M.F. & ZAMAN, K.B.M.Q. 1978 The free shear layer tone phenomenon and probe interference. *J. Fluid Mech.* **87**, 349–383.

ILAK, M., SCHLATTER, P., BAGHERI, S. & HENNINGSON, D.S. 2012 Bifurcation and stability analysis of a jet in crossflow. *J. Fluid Mech.* **696**, 94–121.

IYER, P.S. & MAHESH, K. 2016 A numerical study of shear layer characteristics for low-speed transverse jets. *J. Fluid Mech.* **790**, 275–307.

KAMOTANI, Y. & GREBER, I. 1972 Experiments on a turbulent jet in a cross flow. *AIAA J.* **10** (11), 1425–1429.

KARAGOZIAN, A.R. 2010 Transverse jets and their control. *Prog. Energy Combust. Sci.* **36**, 531–553.

KELSO, R.M., LIM, T.T. & PERRY, A.E. 1996 An experimental study of round jets in cross-flow. *J. Fluid Mech.* **306**, 111–144.

KUZO, D.M. 1995 An experimental study of the turbulent transverse jet. PhD thesis, California Institute of Technology.

LISCINSKY, D.S., TRUE, B. & HOLDEMAN, J.D. 1995 Effects of initial conditions on a single jet in crossflow. *AIAA Paper* 95-2998.

MAHESH, K. 2013 The interaction of jets with crossflow. *Annu. Rev. Fluid Mech.* **45**, 379–407.

MARGASON, R.J. 1993 Fifty years of jet in cross flow research. AGARD-CP-534, Vol. 1, Neuilly sur Seine, France, 1–141.

MARZOUK, Y.M. & GHONIEM, A.F. 2007 Vorticity structure and evolution in a transverse jet. *J. Fluid Mech.* **575**, 267–305.

M'CLOSKEY, R.T., KING, J., CORTELEZZI, L. & KARAGOZIAN, A.R. 2002 The actively controlled jet in crossflow. *J. Fluid Mech.* **452**, 325–335.

MEGERIAN, S., DAVITIAN, J., ALVES, L.S.D.B. & KARAGOZIAN, A.R. 2007 Transverse-jet shear-layer instabilities. Part 1. Experimental studies. *J. Fluid Mech.* **593**, 93–129.

MEYER, K.E., PEDERSEN, J.M. & ÖZCAN, O. 2007 A turbulent jet in crossflow analysed with proper orthogonal decomposition. *J. Fluid Mech.* **583**, 199–227.

MICHALKE, A. 1971 Instabilitat eines kompressiblem ruden friestrahls unter beruck-sichtingung des einflusses der strahlgrenzschichtdicke. *Z. Fluzwiss* **9**, 319–328.

PETERSEN, R.A. & SAMET, M.M. 1988 On the preferred mode of jet instability. *J. Fluid Mech.* **194**, 153–173.

PETERSON, S.D. & PLESNIAK, M.W. 2004 Evolution of jets emanating from short holes into crossflow. *J. Fluid Mech.* **503**, 57–91.

REGAN, M.A. & MAHESH, K. 2017 Global linear stability analysis of jets in cross-flow. *J. Fluid Mech.* **828**, 812–836.

REGAN, M.A. & MAHESH, K. 2019 Adjoint sensitivity and optimal perturbations of the low-speed jets in cross-flow. *J. Fluid Mech.* **877**, 330–372.

SCHLATTER, P., BAGHERI, S. & HENNINGSON, D.S. 2011 Self-sustained global oscillations in a jet in crossflow. *Theor. Comput. Fluid Dyn.* **25**, 29–146.

SHAN, J. & DIMOTAKIS, P. 2006 Reynolds-number effects and anisotropy in transverse-jet mixing. *J. Fluid Mech.* **566**, 47–96.

SHOJI, T. 2017 Mixing and structural characteristics of unforced and forced jets in crossflow. PhD dissertation, University of California, Los Angeles.

SHOJI, T., BESNARD, A., HARRIS, E.W., M'CLOSKEY, R.T. & KARAGOZIAN, A.R. 2019 Effects of axisymetric square-wave excitation on transverse jet structure and mixing. *AIAA J.* **57** (5), 1862–1876.

SHOJI, T., HARRIS, E.W., BESNARD, A. & KARAGOZIAN, A.R. 2020*a* Effects of sinusoidal excitation on transverse jet dynamics, structure and mixing. *AIAA J.* **58** (9), 3889–3901.

SHOJI, T., HARRIS, E.W., BESNARD, A., SCHEIN, S.G. & KARAGOZIAN, A.R. 2020*b* On the origins of transverse jet shear layer instability transition. *J. Fluid Mech.* **890**, A7.

SIROVICH, L. 1987 Turbulence and the dynamics of coherent structures. *Q. Appl. Maths* **45**, 561–590.

SMITH, S.H. & MUNGAL, M.G. 1998 Mixing, structure, and scaling of the jet in crossflow. *J. Fluid Mech.* **357**, 83–122.

STRYKOWSKI, P.J. & NICCUM, D.L. 1991 The stability of countercurrent mixing layers in circular jets. *J. Fluid Mech.* **227**, 309–343.

SU, L.K. & MUNGAL, M.G. 2004 Simultaneous measurements of scalar and velocity field evolution in turbulent crossflowing jets. *J. Fluid Mech.* **513**, 1–45.

ZAMAN, K.B.M.Q. 1998 Reduction of jet penetration in a cross-flow by using tabs. In *34th AIAA/ASME/SAE/ASEE Joint Propulsion Conference and Exhibit*, American Institute of Aeronautics and Astronautics, pp. 3276–3284. AIAA-98-3276.

ZAMAN, K.B.M.Q. & FOSS, J.K. 1997 The effect of vortex generators on a jet in a cross-flow. *Phys. Fluids* **9** (1), 106–114.

ZAMAN, K.B.M.Q. & MILANOVIC, I. 2012 Control of a jet-in-crossflow by periodically oscillating tabs. *Phys. Fluids* **24**, 055107.

ZAMAN, K.B.M.Q., REEDER, M.F. & SAMIMY, M. 1991 Effect of tabs on the evaluation of an axisymmetrical jet. NASA Technical Memorandum NASA-TM104472.

ZAMAN, K.B.M.Q., REEDER, M.F. & SAMIMY, M. 1992 Supersonic jet mixing enhancement by delta tabs. *AIAA Paper* 92-3548.

ZAMAN, K.B.M.Q., REEDER, M.F. & SAMIMY, M. 1994 Control of an axisymmetric jet using vortex generators. *Phys. Fluids* **6** (2), 778–793.